applied sciences

MDPI

Article

Tunable Cellular Structures with Damping for Industry-Ready Dynamic Load Management in Bus Applications

Tiago Cunha [1], Nuno A. T. C. Fernandes [2,*], Delfim Soares [2] and Óscar Carvalho [2,3,*]

[1] Department of Mechanical Engineering, University of Minho, 4800-058 Guimarães, Portugal
[2] Center for Microelectromechanical Systems (CMEMS), University of Minho, 4800-058 Guimarães, Portugal; dsoares@dem.uminho.pt
[3] Associate Laboratory in Biotechnology and Bioengineering and Microelectromechanical Systems (LABBELS), University of Minho, 4800-058 Guimarães, Portugal
* Correspondence: nnunofernandes@dem.uminho.pt (N.A.T.C.F.); oscar.carvalho@dem.uminho.pt (Ó.C.)

Featured Application

This work presents tunable cellular structures with integrated damping designed to manage dynamic loads in bus applications, addressing key industry challenges related to vibration, shock, durability, and passenger comfort. By leveraging geometry-driven mechanical tuning and energy dissipation at the structural level, these lightweight and modular systems can be adapted to target specific frequency ranges associated with road excitation, suspension dynamics, and powertrain vibrations. The structures are compatible with scalable manufacturing techniques, including additive manufacturing, enabling straightforward integration into existing bus platforms or retrofitting into legacy systems. Beyond performance gains, the proposed solution enhances component lifespan, reduces maintenance requirements, and supports sustainability goals through material efficiency and recyclability, positioning it as an industry-ready approach for next-generation public transport dynamic load management.

Abstract

Sustainable mobility has been an emerging topic in recent years, and in this regard, investing heavily in public transport seems to be the best solution. For people to embrace this form of mobility, services must meet expectations, and one of the parameters to be considered is the comfort offered by vehicles. This is directly affected by the vibrations that affect vehicles. This work was developed to create a proof of concept for a support structure for bus seats that mitigates the vibrations felt by passengers, making these vehicles more comfortable and appealing to use. Current systems are expensive and complex, and the proposed solution presented here is based on the field of metamaterials. This study investigated vehicle dynamic loads and comfort standards from ISO 2631 to design a metamaterial-based seat support with optimized stiffness and damping. Using MATLAB (R2024b), ideal parameters were defined (k = 13,422.66 N/m, c = 534.07 Ns/m), with stiffness provided by the cell geometry and damping provided by a viscoelastic material. Parametric modeling and simulations in ANSYS (2025 R2) assessed stiffness, damping, and strength, followed by prototype fabrication and testing. The best structure showed 2.23 m/s^2 at 4.5 Hz, achieving the target transmissibility above 8 Hz. While most designs effectively attenuate vibrations beyond 5 Hz, resonance peaks remain high, suggesting future work should focus on improved resonance reduction strategies.

Check for updates

Academic Editor: Yuval Cohen

Received: 23 January 2026
Revised: 6 February 2026
Accepted: 9 February 2026
Published: 11 February 2026

Copyright: © 2026 by the authors. Licensee MDPI, Basel, Switzerland. This article is an open access article distributed under the terms and conditions of the Creative Commons Attribution (CC BY) license.

Keywords: comfort; damping; metamaterials; transmissibility; vibrations; bus; industry-ready; vibration control

1. Introduction

The paradigm of daily mass mobility has been undergoing profound changes. Nowadays, there has been an increase in investment in public transport, electric mobility, and in reducing private cars. In the European Union alone, for example, the transport infrastructure program under the Connecting Europe Facility (CEF) for 2021–2027 was allocated approximately €25.8 billion in public funding. Moreover, analysts estimate that to develop a green-transport manufacturing base and meet decarbonization goals, the EU must commit around €39 billion per year in public investment [1]. Recently, the Portuguese Government announced an investment of 240 € million for the construction and improvement of public transport networks in Lisboa, Porto, and Coimbra [2]. This investment is part of the Sustainable 2030 program, which has 2.7 € billion for mobility projects [3]. The "Programa Nacional de Investimentos 2030" for transport envisages that 56% of this investment will be in urban mobility and railways [4]. The motivations for these changes are varied, including environmental concerns, excessive traffic in cities, and increased demand due to rising fuel prices, among others. According to the Green Paper–Towards a New Culture of Urban Mobility report, prepared by the European Commission [5], it is important to promote the implementation, extension, and/or rehabilitation of "green" means of transport, such as trains, metros, and buses. It should be noted that, in Portugal, railways are responsible for only 1% of CO_2 emissions [4]. In the European Union, in 2019, road transport accounted for 72% of all CO_2 emissions from transport, of which 61% corresponded to private cars [6]. The future of mobility is, thus, strongly directed towards public transport networks by road (buses, shared light vehicles) and rail (trains and subways) for common day-to-day travel.

For there to be a transition in the mobility paradigm, it is necessary that the new proposals (trains, buses, and metros) are as, or more, inviting to use when compared to private vehicles. Among many other parameters [7], the importance of comfort is highlighted. Among the various factors that affect this parameter, the effect of vibrations stands out, whose associated discomfort can influence the well-being of passengers in different ways. A significant proportion of public transport users take advantage of their travel time to carry out various activities, such as reading, chatting, sleeping, making calls, working on their computers, and studying [8–10]. The effect of vibrations can compromise the ability to perform such activities, as prolonged or excessive exposure degrades comfort, concentration, and motor performance. Beyond immediate functional impairment, vibration exposure has been shown to influence passenger health by inducing complex mechanical waves that propagate through the human body. These waves interact with biological tissues in a frequency, amplitude, and direction-dependent manner, potentially affecting musculoskeletal structures, soft tissues, and even neurological response. Consequently, there has been growing scientific interest in understanding human–vibration interaction through a combination of in silico numerical models [11,12], physical medical phantoms [13–15], and controlled experimental studies [16]. Computational approaches enable detailed investigation of wave propagation and tissue-level stress distributions, while biofidelic phantoms and experimental measurements provide essential validation and insight into realistic human response, or even for the development of medical devices [17]. Together, these complementary methodologies form a robust framework for assessing the short- and long-term effects of vibration exposure on human health. Thus, the concept of Whole Body Vibration (WBV) can be defined as the set of mechanical vibrations

that is transferred to the human body as a whole, and which, in certain situations, may pose risks to the health and safety of those who are subject to this phenomenon [18]. The methods for assessing human exposure to the WBV phenomenon are determined by the ISO 2631:1-1997 standard [19]. It defines the permissible parameters of vibration that human beings can withstand without endangering their condition, as well as methods of calculating and evaluating these parameters. According to several studies, prolonged exposure to WBV is intrinsically associated with the development of musculoskeletal pain in the back, neck, hands, shoulders, and legs [11,13–15]. In particular, the lumbar region is sensitive to frequencies between 4 and 10 Hz, and therefore, exposure to vibrations in this frequency range and high amplitude can lead to pain in this region and the development of diseases in the joints of the spine [20]. Different frequency ranges act on different parts of the human body: between 5 and 10 Hz, the most affected area is the chest and abdominal area; between 20 and 30 Hz, the head, neck, and shoulder region; and in the range of 30 to 60 Hz, the ocular system [21,22]. Typical vibrations in a car typically go up to 30 Hz [23].

To mitigate the vibrations felt by users, this type of vehicle has suspensions between the wheels and the body of the vehicle. However, these systems absorb only part of the vibrations (mainly higher frequencies), so low-frequency impacts and vibrations are still transmitted to passengers [20]. Therefore, the main solutions taken are the use of suspension systems in the seats of drivers, since they are the most vulnerable agents exposed to WBV, precisely because of the exposure time. The suspensions currently used in drivers' seats are divided into three groups: passive, active, and semi-active suspensions [21,24,25]. The first group represents the simplest case, in which the attenuation of vibrations of a mass is done using a spring and a shock absorber. The designation represents the fact that it is not possible to add power to the system [25]. These systems are quite simple, inexpensive, and easy to maintain, but their main limitation is the inability to isolate low-frequency vibrations [25]. Active suspensions arose due to the inability of passive suspensions to reach their full potential in terms of vibration attenuation, and therefore, are not being fully efficient [26]. They use electromagnetic, hydraulic, and/or pneumatic systems to actively generate, i.e., at the exact moment, compensating forces that cancel out the accelerations caused by vibrations. Active systems are more efficient at reducing vibration transmission [21]. Finally, the group of semi-active suspensions is the intermediate case of the two previous ones, and several solutions arise in this context since active suspensions require high actuation power, are complex, and have high costs [25], and passives prove to be inefficient [19,20]. Recent advances in vehicle vibration mitigation have largely focused on active and semi-active suspension systems, where control strategies such as skyhook, groundhook, and inertial suspension concepts are employed to improve ride comfort and road friendliness across a wide frequency range. For example, Yang et al. demonstrated that combining inertial suspension structures with semi-active control strategies can effectively enhance vibration isolation performance, particularly by addressing phase deviation effects inherent to conventional control approaches [27–29]. These systems can use active shock absorbers, i.e., those that vary the force–velocity ratio according to the applied load, or air regulation in air springs [25]. This group also includes systems that use electro and magnetorheological characteristics [14,20]. Systems that use negative stiffness elements have also been used, in which certain components reduce the overall stiffness of the system, increasing the insulation efficiency. These systems combine high static stiffness with low dynamic stiffness, ideal situations, respectively, for when the vehicle is stationary and moving, and have low costs and simplicity [18,19].

It is true that several solutions have already been proposed, and others are being developed, to prevent the transmission of vibrations from the vehicle structure to the seats, especially to the driver. However, these solutions represent high levels of complexity and

cost; these solutions can be justified for implementation in drivers' seats, given that they are exposed to WBV more intensely than passengers and only one system is required in each vehicle (or two, for railway vehicles with two driver's cabs). Nevertheless, there remains a significant gap in the literature regarding the development of vibration mitigation systems that are industry-ready, cost-effective, and suitable for widespread passenger use. Existing studies tend to focus either on highly specialized driver-assist suspension mechanisms or on theoretical metamaterial configurations that have yet to be translated into scalable, manufacturable products. Thus, this work explores the possibility of developing a system based on metamaterials capable of attenuating vibrations purely through its structural configuration, offering a simpler, maintenance-free, and potentially low-cost alternative for passenger comfort enhancement.

The word "metamaterial" has in its constitution the prefix meta, which is of Greek origin and has the meaning "beyond" [21,22]. This means, therefore, that a metamaterial will be something that goes beyond conventional materials, in the sense that it is possible to obtain properties that they do not have [30,31]. Metamaterials can be divided into several groups, taking into account their properties, i.e., mechanical, electromagnetic, acoustic, and thermal [31–33]. In the groups mentioned above, mechanical metamaterials are the ones of greatest interest to this study. These were developed later [32], and their design is focused on obtaining structures with certain properties to respond to mechanical, static, and/or dynamic stresses [23,24]. In other words, the response of the material does not depend on the properties conferred by its chemical composition and microstructure, but rather on the structural configuration elaborated [23,26,27]. Mechanical metamaterials have applications in several areas of engineering. Their energy absorption capacity is high, as they can distribute energy and reduce the maximum impact stress [33], which allows for its application in military equipment and in personal and vehicle protection systems. They also have great applicability in vibration and sound isolation of machines and vehicles, which inherently allows for obtaining reduced mass systems [34–36]. It is possible to obtain lightweight structures with high stiffness that depend only on the designed geometry [20], which, therefore, gives a high specific stiffness.

Several authors have studied various applications ranging from vibration damping to energy absorption, formation of isolation bands, and seismic protection. However, further developments need to be made to attempt to apply metamaterials to improve the dynamic comfort of public transport. Thus, what is intended in this work is to develop a structure capable of attenuating the vibrations felt by passengers, and metamaterials have the great advantage of being designed for a certain set of mechanical properties. In addition, it is important to favor an economical, low-maintenance, and industrializable solution. This last parameter is important so that there can be a practical application of the solution.

2. Theory

2.1. Vibration Theory

A one-degree-of-freedom dynamic system, in its elementary form, can be reduced to a mass, a spring, and a damper. For the application in question, the mass is supplied by the passenger's body (and other bodies, such as the seat, luggage, etc.). Stiffness, k, and damping, c, will be provided by the structure to be developed. Notice, for example, the typical suspension of a car, in which the mass is the vehicle's chassis and the rigidity and damping are given by the elements that connect the chassis to the wheel, which are the spring and the shock absorber, respectively.

When a disturbance is applied to the mass, the system responds to the request according to the equation of motion. However, the case presented consists of a base excitation,

since the perturbing force is not applied to the mass, but to the base of the system. In this case, the equation of motion is modified into Equation (1):

$$m\ddot{x} + c(\dot{x} - \dot{y}) + k(x - y) = y(t) \quad (1)$$

where $y(t)$ is the base displacement, $k(x - y)$ is the elastic restoring force relative to the base, and $c(\dot{x} - \dot{y})$ is the damping relative to base motion.

To measure the efficiency of a vibration attenuation system where there is excitation at the base, a parameter called transmissibility, T, is used, which measures the ratio between the response amplitude of the system and the excitation amplitude [37], and which indicates the ability of the material to efficiently mitigate a given dynamic load. This parameter is calculated through Equation (2):

$$T = \frac{x}{y} = \sqrt{\frac{1 + (2\xi\beta)^2}{(1 - \beta^2)^2 + (2\xi\beta)^2}} \quad (2)$$

where x and y represent, respectively, the displacements in and out of the system. β represents the ratio of frequencies, calculated as shown in Equation (3). The system resonates when $\beta = 1$ and vibration isolation—transmissibility lower than 1—is achieved when $\beta > \sqrt{2}$ [38]:

$$\beta = \frac{\omega_d}{\omega_n} \quad (3)$$

where ω_d and ω_n represent, respectively, the natural angular frequency and the damped natural frequency, calculated by Equations (4) and (5). Notice, by Equation (4), the lower the stiffness k and the lower the natural frequency ω_n of the mass system m:

$$\omega_n = \sqrt{\frac{k}{m}} \quad (4)$$

$$\omega_d = \sqrt{1 - \xi^2}\omega_n \quad (5)$$

ξ is the damping factor, obtained according to Equation (6):

$$\xi = \frac{c}{c_{crit}} = \frac{c}{2\sqrt{km}} = \frac{c}{2m\omega_n} \quad (6)$$

where c represents the damping coefficient and c_{crit} represents the critical damping of the system, which corresponds to the c value of the system, after the disturbance, and returns to the equilibrium point in the shortest possible time, without oscillating.

2.2. Spring

It is possible to vary the stiffness of metamaterials in the same way that one varies the stiffness of a beam. This parameter indicates the resistance that a material, structure, or component presents to a deformation, δ, when a load F is imposed on it [39].

Of course, the concept of a spring is not applied in its literal sense. Stiffness is given by elements that are, for example, found in bending. Each unit cell can be designed with a set of blades, whose stiffness value can be calculated according to Equation (7):

$$k = \frac{3EI}{L^3} \quad (7)$$

where E represents the Young's modulus of the material, I represents the moment of inertia of the cross-section of the beam, and L represents the length. This means that the stiffness

of the beam depends on the selected material and geometry, parameters that are also important for the analysis of installed stresses, as shown below in Equation (8):

$$\sigma = \frac{Mr}{I} = \frac{FLr}{I} \quad (8)$$

where M represents the bending moment, F represents the load, and c represents the distance to the neutral axis. The material data does not enter directly into the calculation, but it is necessary to compare the installed stress with the maximum admitted stress of the material to prevent yield. It is also possible to manipulate stiffness by assembling stiffness elements in parallel and/or in series. It should be remembered that, in the first case, the displacement is the same for all springs, and the applied load is subdivided between them [40]. This reinforces the idea that it is possible to manipulate the stiffness of a metamaterial more easily, through the design and association of elements in parallel or in series, depending on the need to increase or decrease the overall stiffness of the system.

2.3. Damper

For the dissipation of the potential energy accumulated in the springs, a dissipation source is required, represented by a damper. In this work, damping is implemented through viscoelasticity and constrained layer damping (CLD) made of silicone rubber. This way of dissipating energy is due to the alternating movement in a slice of a layer of viscoelastic material that is constrained between two more rigid layers (Figure 1), which have relative movement in relation to each other [41]. Energy is dissipated in the form of heat [42].

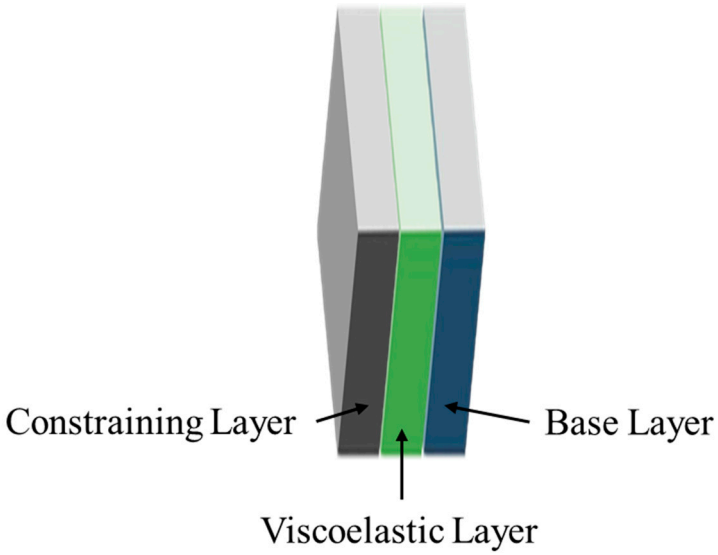

Figure 1. Concept of constrained layer damping.

The dimensions of the layers can be designed to dampen certain frequencies, and are intended for various applications, from small insulator systems to railway vehicle wheels [43]. The core material, due to its viscoelastic nature, has a complex Young's modulus and is dependent on parameters such as frequency and temperature [44]. In the structure developed in this work, the silicone layer will be placed in parallel with the spring, in each of the cells. According to Shu, You and Zhou [45], viscoelastic materials have been gaining importance in the area of vibration attenuation. According to these authors, this type of material has a great dissipative capacity, represented by a high loss factor, low heat production, and good heat dissipation, stability, and durability in different environments, temperatures, and working conditions. Also in this study, it was concluded

that silicone rubber, despite not being the elastomer with the highest dissipative capacity, has a high shear modulus and lower sensitivity to temperature and frequency variations.

The behavior of a viscoelastic material is a conjunction of an elastic response, described by Hooke's law, where the normal stress is proportional to the strain, with a viscous response, described by Newton's law, where the shear stress is proportional to the strain rate [42]. The most important properties of this type of material are the complex Young's modulus and the loss factor [43]. In this way, the complex modulus E^* is described according to Equation (9) [35,38]:

$$E^* = E' + jE'' \tag{9}$$

where E_s represents the storage modulus (elastic part, which represents the accumulation of energy) and E_l represents the loss modulus (viscous part, which represents the dissipation of energy) [39,40]. These parameters have a strong frequency dependence [46,47], and relate to each other through the loss factor, γ, according to Equation (10):

$$\tan\gamma = \frac{E''}{E'} \tag{10}$$

This constant corresponds to the angle of lag of the response between the installed stress and the applied strain [48,49], and represents the part of the energy that is dissipated with cyclic motion [47]. That is, in a sinusoidal movement, the stress and strain also present a sinusoidal response, with the same angular frequency, but with a lag γ [50]. Considering that viscosity assumes a linear behavior, i.e., only the dependence of the material's response on frequency and temperature (excluding the strain amplitude) is considered [43], the complex cutting modulus, G^*, can be related to the complex Young's modulus as follows in Equation (11) [41]:

$$G^* = \frac{E^*}{2(1+\nu)} \tag{11}$$

where ν represents Poisson's coefficient.

3. Materials and Methods

3.1. Problem Definition

To correctly solve the problem, it is necessary to know the dynamic loads that reach the passengers' seats. Melo [51], in his doctoral thesis, analyzed whole-body vibrations of bus drivers and, to this end, his research focused on studies by Paddan and Griffin [44,45]. The collection revealed vertical acceleration values that reach users' seats between 0.44 and 0.56 m/s^2. From these data, an average vertical acceleration value of 0.5 m/s^2 was considered. This acceleration value, according to ISO 2631 [19], is positioned on the threshold of the "slightly uncomfortable" and "reasonably uncomfortable" levels, as can be seen in Figure 2.

Since the primary objective of this study is to enhance passenger comfort, the design target is to maintain the accelerations experienced by the occupant within the "comfortable" level, that is, less than 0.315 m/s^2. According to Equation (2), the corresponding transmissibility value is obtained in Equation (12):

$$T = \frac{\ddot{x}}{\ddot{y}} = \frac{0.315\ \text{m/s}^2}{0.5\ \text{m/s}^2} = 0.63 \tag{12}$$

In order to obtain stiffness and damping values, the appropriated value of ξ for the passengers' comfort was fixed. For this, the literature regarding the common values of this parameter was analyzed. In a study carried out by Susatio et al. [52–54], the value of the damping factor was estimated for the development of an active suspension system. The

authors thus obtained values between 0.21 and 0.22. Calvo, Díaz and Román [55], in a work inspecting the dynamic behavior of the suspension of vehicles, presented damping factor values between 0.20 and 0.25 for comfortable cars. Thus, a damping factor of 0.25 was defined for the system developed in this work. Another important aspect is the height of the structure, which should not exceed 600 mm, in order to maintain the height from the floor that the seats currently have.

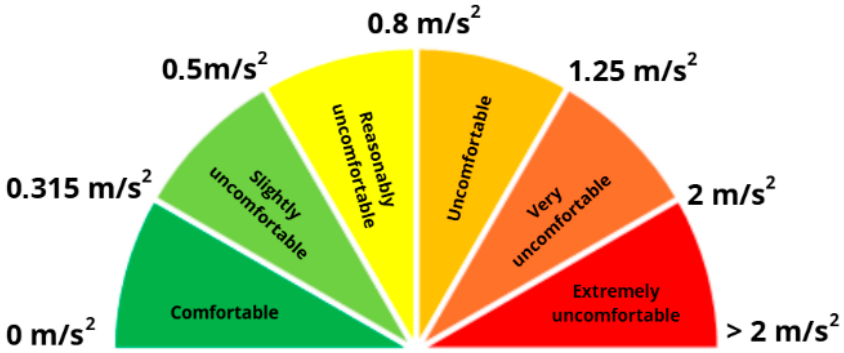

Figure 2. Comfort levels defined by ISO 2631.

In this study, a generic and representative bus configuration under nominal loading conditions was adopted as an illustrative case, following common practice in vibration and ride-comfort studies, where simplified vehicle models are used to evaluate isolation concepts independently of specific passenger load variations [56–58].

3.2. Conceptual Design

Considering some examples present in the analyzed literature, a sketch of a unit cell for the structure is presented in Figure 3. The spring and damper (respectively the blades and the viscoelastic material) are mounted in parallel. The cell is symmetrical according to the central vertical plane. The placement of several blades on each column represents a series of springs, which will lead to a reduction in overall stiffness. The final configuration and dimensions of the cell were adjusted considering the installed stress values, obtained through computer simulations. The geometry was designed in this way so that it would be possible to prototype it by additive manufacturing (FDM) and for future industrialization processes.

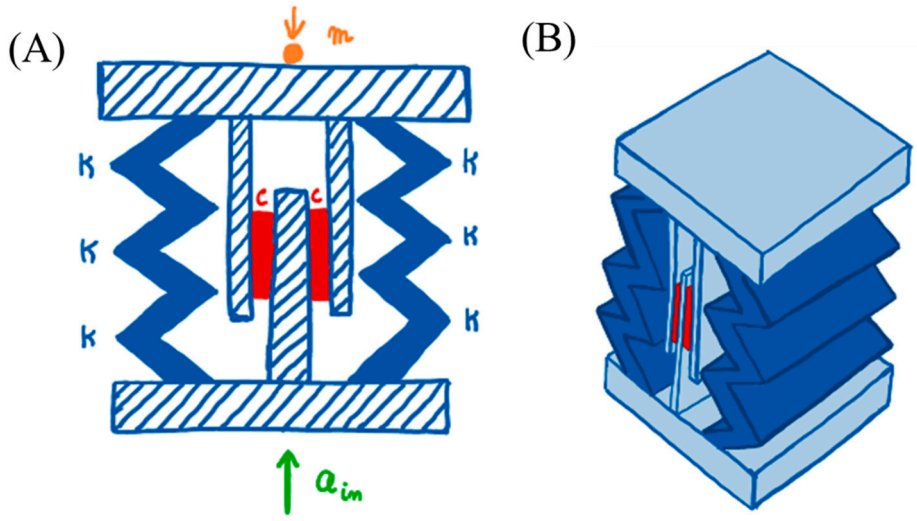

Figure 3. Sketch made for the unit cell: (**A**) section view and (**B**) isometric view.

3.3. Materials' Definition

3.3.1. Stiffness

The literature analyzed considers several polymer options for FDM and injection manufacturing, with those that were most discussed being PLA, ABS, and TPU. The selection was made by taking into account parameters such as Young's modulus, yield stress, and ease of printing, as presented in Table 1 [59–61].

Table 1. Young's modulus, yield stress, and ease of printing of the analyzed materials.

Material	Young's Modulus	Yield Stress	Ease of Printing	Bibliographic Reference
ABS	1.47 GPa	38.4 MPa	Medium	[53]
PLA	2.50 GPa	36.0 MPa	High	[59–61]
TPU	4.91 GPa	35.0 MPa	Low	[59–61]

Analyzing these parameters, it is possible to see that TPU is much stiffer than other materials (3.34 times stiffer than ABS and 1.96 times stiffer than PLA), and its yield stress is the lowest, which leads to discarding this material. It should be noted that it is important that the stiffness of the material is low to obtain a low natural frequency of the system. In addition, of the three proposals, it is the one that reveals the greatest difficulty in printing. Between the remaining two materials, the possibility of using PLA was initially considered, due to the ease of printing. However, it was necessary to opt for ABS, since the stiffness of PLA proved to be excessive when obtaining the ideal value of k, combined with the tension installed in the structure. The material was defined in the *Ansys (2025 R2)* isotopically, that is, its properties are equal in all directions [61–63]. Thus, values were defined for the specific mass, Young's modulus, and Poisson ratio, as presented in Table 2.

Table 2. ABS Properties Defined in *Ansys (2025 R2)*.

Property	Specific Mass	Young's Modulus	Poisson Ratio
Value	1050 kg/m^3	1.4 GPa	0.3

3.3.2. Damping

The material selected for damping is RTV-2 (Room Temperature Vulcanization) silicone rubber. This is a viscoelastic material, widely used in CLD applications [43], such as in the aeronautical industry [46]. To obtain the values of the storage and loss moduli, DMA tests were performed (*dynamic mechanical analysis*) [38,42] on a small sample of material with dimensions 25 × 8 × 5 mm. The test was carried out at four frequencies—1, 10, 50, and 100 Hz—with a gradual increase in temperature. Thus, the test made it possible to obtain the storage and loss moduli and also the tan γ, as the frequency and temperature are varied. The values considered for the calculation of the Prony series were those with the lowest temperature, and that were closer to the ambient temperature. The complex shear modulus, G^*, is obtained by calculating the effective value between the storage modulus and the loss modulus.

3.4. Numerical Methods

3.4.1. Parameter Analysis for Ideal Stiffness and Damping Using Matlab

For the calculation of the damping and stiffness parameters, and considering the specifications described, a *Matlab (R2024b)* code was elaborated, with the aim of finding the natural frequency of the system that imposes a mass response with a transmissibility

in the selected range (0 to 25 Hz) that is less than 0.63 to the greatest extent possible and minimizes peak resonance (Figure 4).

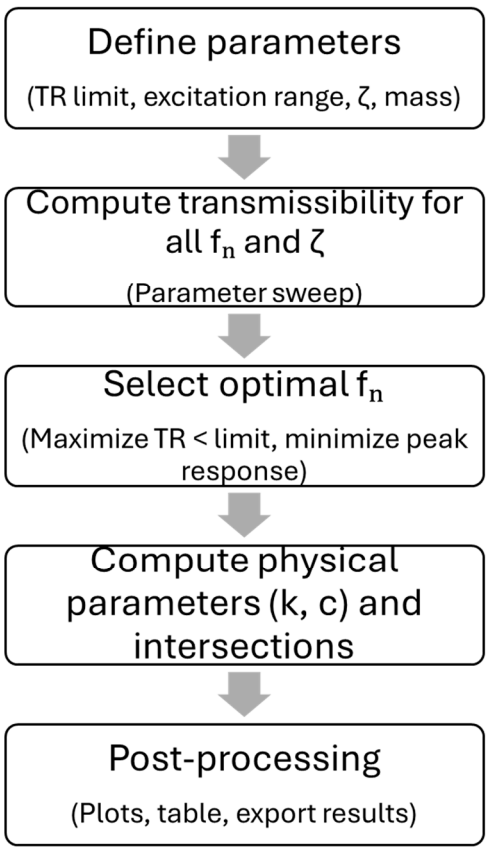

Figure 4. Flowchart of the numerical optimization procedure used to identify optimal stiffness and damping parameters based on transmissibility criteria.

The procedure begins with the definition of the key inputs, including the transmissibility limit, excitation frequency range, damping ratio values, and system mass. A parametric sweep is then performed, computing the vibration transmissibility for all combinations of natural frequency and damping ratio. Based on these results, the optimal natural frequency is selected by maximizing the frequency range for which transmissibility remains below the prescribed limit, while simultaneously minimizing the peak response. The corresponding physical parameters, namely stiffness and damping, are subsequently calculated, along with the identification of relevant transmissibility intersections. Finally, the results are post-processed to generate plots, summary tables, and exported datasets for further analysis and reporting.

It is known that transmissibility is only less than unity when the excitation frequency reaches the value of $\omega_n\sqrt{2}$, and, as this is a range of low frequencies, it is important that the natural frequency is as low as possible.

Equation (2) was modified to the frequency domain, so that frequency and ζ could be used as input parameters, as is shown in Equation (13):

$$|T(\omega)| = \sqrt{\frac{1 + \left(2\zeta\frac{\omega}{\omega_n}\right)^2}{\left(1 - \frac{\omega}{\omega_n}^2\right)^2 + \left(2\zeta\frac{\omega}{\omega_n}\right)^2}} \quad (13)$$

The MATLAB script performs a parametric optimization of a single-degree-of-freedom vibration isolation system, aiming to identify the ideal combinations of stiffness (k) and

damping coefficient (c) that minimize the transmission of vibrations to passengers. For a range of damping ratios and natural frequencies, the code computes the vibration transmissibility across a given excitation frequency spectrum using the classical transmissibility model. It then evaluates which configurations maintain TR below the comfort threshold (0.63, as defined by ISO 2631) over the widest range of excitation frequencies. The corresponding optimal natural frequency, stiffness, and damping values are then extracted and plotted, providing insight into how different damping levels influence comfort performance.

3.4.2. Stiffness Element Analysis Using Ansys

The blade was modeled on the *Ansys Design Modeler*. This model was elaborated as a unit cell, with two blades in parallel, and its length, height, and thickness were parameterized. Equation (14) represents Hooke's law, and is the one used by the software to calculate stress, where the vector of this variable, $\{\sigma\}$, is given by the product between the stiffness matrix, $[D]$, and the displacement vector, $\left\{\varepsilon^{el}\right\}$:

$$\{\sigma\} = [D]\left\{\varepsilon^{el}\right\} \tag{14}$$

The material selected was ABS. This material was defined as an isotropic material, so the stiffness matrix takes the following form in Equation (15):

$$[D]^{-1} = \begin{bmatrix} \frac{1}{E} & -\frac{\nu}{E} & -\frac{\nu}{E} & 0 & 0 & 0 \\ -\frac{\nu}{E} & \frac{1}{E} & -\frac{\nu}{E} & 0 & 0 & 0 \\ -\frac{\nu}{E} & -\frac{\nu}{E} & \frac{1}{E} & 0 & 0 & 0 \\ 0 & 0 & 0 & \frac{1}{G} & 0 & 0 \\ 0 & 0 & 0 & 0 & \frac{1}{G} & 0 \\ 0 & 0 & 0 & 0 & 0 & \frac{1}{G} \end{bmatrix} \tag{15}$$

Via the *parameter set* of *Ansys (2025 R2)*, the stress and strain values were obtained through static tests. The defined boundary conditions, presented in Figure 5, were a proof load of 20 N (to evaluate the displacement) and a load of 850 N (corresponding to the value defined for the mass for the calculation of the stress) on the upper face, a displacement of zero value in x and z on the same face to limit the displacement in these directions, and a fixed support on the base.

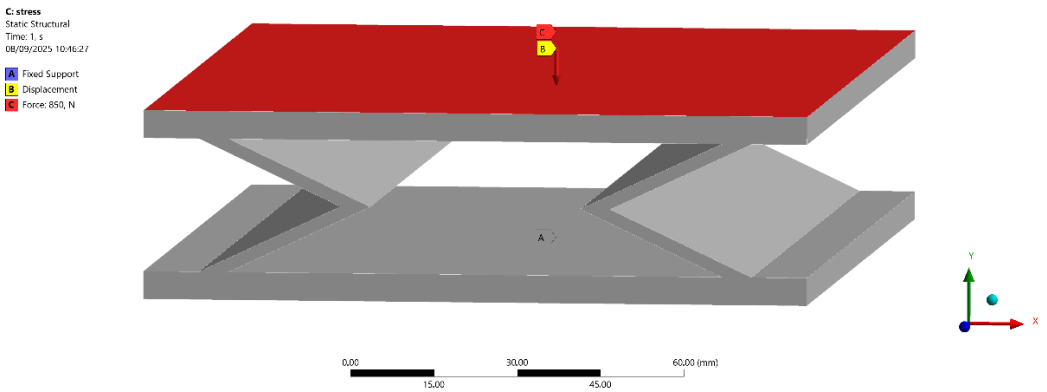

Figure 5. Elaborated geometry of the blade, with the respective definition of the boundary conditions.

3.4.3. Analysis of the Undamped Structure in Ansys

The next phase was to analyze the variation in stiffness with the number of cells and compare these data with the expected theoretical stiffness. The number of cells ranged from 1 to 23. It can be noted, in Figure 6, that the defining boundary conditions in the 10-cell

structure are similar to those defined in the previous section. The cells were joined together by bonded contacts to limit any kind of relative movement.

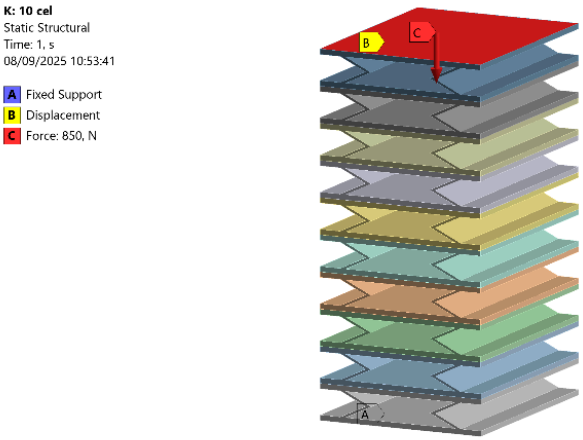

Figure 6. Definition of the boundary conditions for the structure with 10 cells, which are the same for the other cases.

The number of blades per cell was adjusted, considering the buckling behavior, and the value was set to three. After these static validations, some dynamic simulations were performed. The first consisted of a modal analysis of the structure, in which the objective was to extract the first modes of vibration of the structure and to verify whether the first would coincide with the natural frequency obtained in the *Matlab* code. To this end, a point mass of 85 kg was added to the top of the structure, which represents the mass of the passenger and the seat.

Finally, a harmonic response analysis of the structure was carried out, with the objective to "sweep" the amplitude of response of the system (in displacement, velocity, and/or acceleration) along a range of frequencies. In this test, it is intended to verify if the response profile of the system is similar to the curves of the typical transmissibility graph as a function of the frequency ratio. The equation used by the software for this type of simulation is represented in Equation (16):

$$\left(-\Omega^2[M] + i\Omega[C] + [K]\right)(\{u_1\} + i\{u_2\}) = (\{F_1\} + i\{F_2\}) \tag{16}$$

where the matrices $[M]$, $[C]$ e $[K]$ represent the mass, damping, and stiffness matrices, respectively; $(\{u_1\} + i\{u_2\})$ represents the complex displacement vector; $(\{F_1\} + i\{F_2\})$ represents the harmonic stress; and factors Ω of order 0, 1, and 2 represent, respectively, the displacement, velocity, and acceleration. It is possible to transform this equation into a dimensionless parameter equation, taking into account vibration theory, which results in Equation (17):

$$\left(-\Omega^2 + i2\omega_j\Omega\zeta_j + {\omega_j}^2\right)y_{jc} = f_{jc} \tag{17}$$

where ω_j represents the natural frequency of the system, ζ_j is the modal damping factor, y_{jc} is the complex amplitude, and f_{jc} is the complex modal force. The pre-processing of this test began with the definition of the analysis settings, where the frequency range was defined from 0.5 to 25 Hz, and with a solution range number of 100. The solver selected was full harmonic. With the definition of this solver, it is not possible to define an acceleration as a base excitation, and so, to work around this problem, it was defined as a frequency-dependent displacement. Considering the value of the input acceleration, the value of the

displacement was calculated for each frequency between 0 and 25 Hz, in intervals of 0.5 Hz, according to Equation (18):

$$y(f) = \frac{\ddot{y}}{(2\pi f)^2} \tag{18}$$

As described below in Figure 7, the offset was defined tabularly, and the calculated values were entered on the y-axis. An excerpt of the displacement values as a function of frequency can be found in Appendix A.1, Table A1. The selected geometry was the basis of the structure.

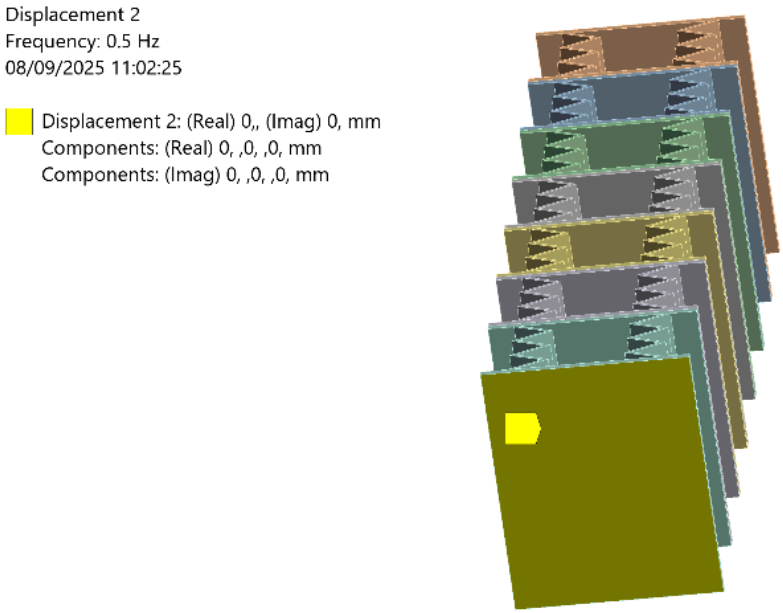

Figure 7. Definition of the displacement as a function of frequency to replace the base excitation acceleration.

The constraints defined in the structure were a zero displacement in x and z, as in the previous simulations, and a frictionless support on the lateral faces to prevent the global buckling of the structure. The mesh has been defined with an element size of 20 mm.

3.4.4. Analysis of the Damped Structure in Ansys

After the validations performed on the undamped structure, it was necessary to complement the unit cell with a region for the inclusion of silicone rubber. This material was placed on each side of the central wall, and was fixed on this wall and on the side walls. The toothed surface of the wall aims to provide a better adhesion of this material, because in the presence of a smooth surface, it would easily disintegrate. For damping analysis and parameterization, two study variables were considered: the width and height of the layers. The first is obtained through the distance between the lateral walls and the central wall, and values between 2 mm and 16 mm were considered, at intervals of 2 mm; the second was evaluated by varying the number of teeth on the surface of the walls filled with silicone, between one and the seven existing ones. This parameter was designated as "cnX", where X represents the number of teeth filled. In Figure 8, it is possible to verify four extreme cases among the 56 studied. The simulations for each of the cases were carried out, with regard to pre-processing, according to the same model as the last harmonic response simulation presented of the structure without damping.

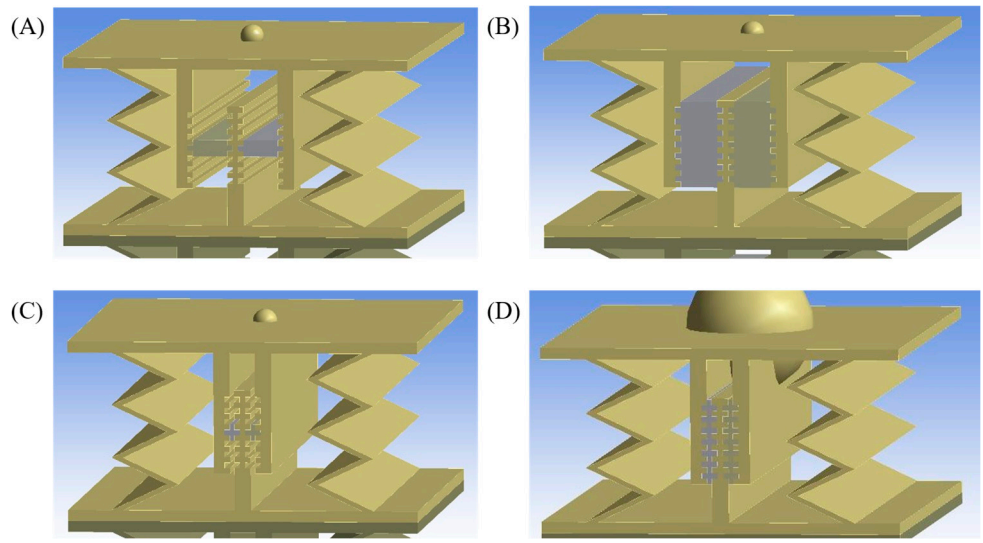

Figure 8. Four extreme cases out of the 56 evaluated, from left to right: (**A**) 16 mm, cn1; (**B**) 16 mm, cn7; (**C**) 2 mm, cn1; and (**D**) 2 mm, cn7.

For the definition of the properties of silicone in *Ansys*, it was necessary to calculate the Prony series [64]. The method allows the definition of a viscoelastic material, since it can represent its behavior in a wide range of times, combined with a good computational efficiency [50]. This formulation can be expressed through Maxwell's model, considering the contribution of each of the elements through a sum [39,53,54] is expressed in Equation (19)

$$G(t) = G_e + \sum_i G_i e^{-t/\tau_i} \tag{19}$$

where t represents time, G_e is the modulus of equilibrium, which represents the response of the material for a long time or for low frequencies, G_i is the modulus of the element i (coefficients of the Prony series), and τ_i is the relaxation time of that same element [65,66]. Equation (19) is the basis of the Prony series, and can be used for its implementation in simulation software [47]. From it, it is possible to obtain the equations that allow the calculation of the storage and loss moduli as a function of frequency [67], expressed in Equations (20) and (21):

$$G'(\omega) = G_e + \sum_i \frac{G_i \omega^2 \tau_i^2}{1 + \omega^2 \tau_i^2} \tag{20}$$

$$G''(\omega) = \sum_i \frac{G_i \omega^2 \tau_i^2}{1 + \omega^2 \tau_i^2} \tag{21}$$

To define material parameters in *Ansys*, it is necessary to perform a *curve fitting* on the moduli's data obtained in the tests, using a mathematical modeling software (*Matlab*, for example) [50]. To do this, the values of τ_i and G_i, and the number of terms that depend on the needs of the curve-fitting operation, are required. The parameters τ_i and g_i will be placed in the software, with the latter obtained by Equation (22):

$$g_i = \frac{G_i}{G_0} \tag{22}$$

The Denominator G_0 Represents the Modulus of Relaxation at the instant $t = 0$.

3.5. Experimental Methods

3.5.1. Experimental Dynamic Mechanical Analysis (DMA)

Dynamic mechanical analysis (DMA) was carried out using a TA Instruments Q800 V21.2 apparatus. Two specimens were prepared following the ASTM D7028 standard [68], with nominal dimensions of 27 mm × 6 mm × 2 mm (length × width × thickness). Tests were conducted in multi-frequency stress mode under a three-point bending configuration, with an oscillation amplitude of 5.0 µm and frequencies ranging from 1 to 100 Hz. The temperature was varied from 28 °C to 47 °C during the measurements. Both the storage (elastic) and loss (viscous) moduli were recorded, providing insight into the frequency- and temperature-dependent viscoelastic behavior of the samples.

3.5.2. Prototype Manufacturing

In order to carry out experimental validation, a prototype of one of the cells of the structure was elaborated. This cell was manufactured by FDM. The printer used was the Creality Ender-3 Pro (Shenzhen, China). This equipment has a printing space of 220 × 220 × 250 mm and allows maximum temperatures in the extrusion nozzle and on the table of 255 °C and 110 °C, respectively. The best unit cell based on the preliminary results was chosen for evaluation. From the Inventor CAD model, a ".stl" file was exported, which is required for pre-processing the print in the UltiMaker Cura software. The printing parameters can be found in Appendix A.2, Table A2.

The next step was to place the silicone rubber in the center of the cell. Since the test cell does not have the elastomer zone fully filled, it was necessary to limit the fill zone. Subsequently, the silicone was poured until the entire region was filled, and healing occurred within the next 24 h. The cell-silicone set produced has a mass of 327.99 g, of which 270.00 g are from the polymer. In Figure 9, the built prototype is represented.

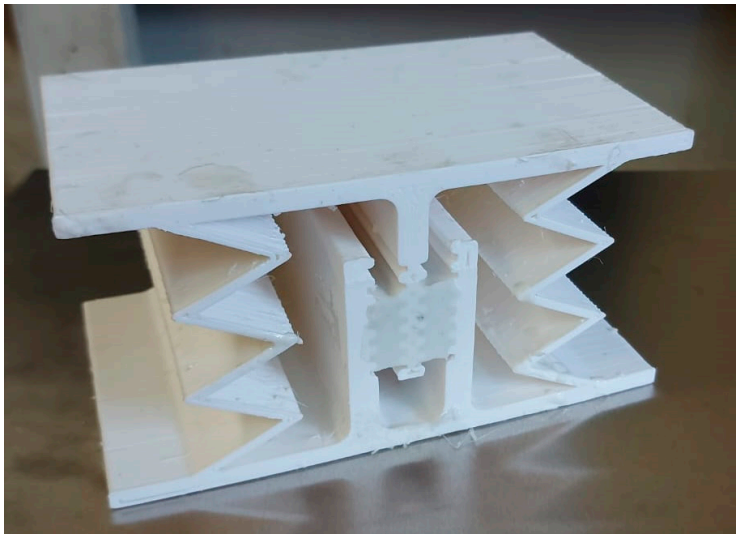

Figure 9. Prototype manufactured for experimental tests.

3.5.3. Experimental Harmonic Mechanical Analysis

The equipment used was a *Mecmesin OmniTest-10* universal testing machine, with a 10 kN load cell. The prototype was placed at the base of the machine, between two metal elements that could house the upper and lower surfaces of the machine, in order to promote a uniform distribution of the load over the entire surface. In the tethering of the machine, a compressor element was mounted to exert the effort on the cell. Figure 10 represents a diagram of the prototype assembly on the test equipment. The main objective of the tests was to obtain the hysteresis curve of the cell. To this end, nine tests were carried out at

different frequencies: the first at 0.5 Hz, the second at 1 Hz, and the following at intervals of 1 Hz from this value. The applied displacement amplitude was 1 mm.

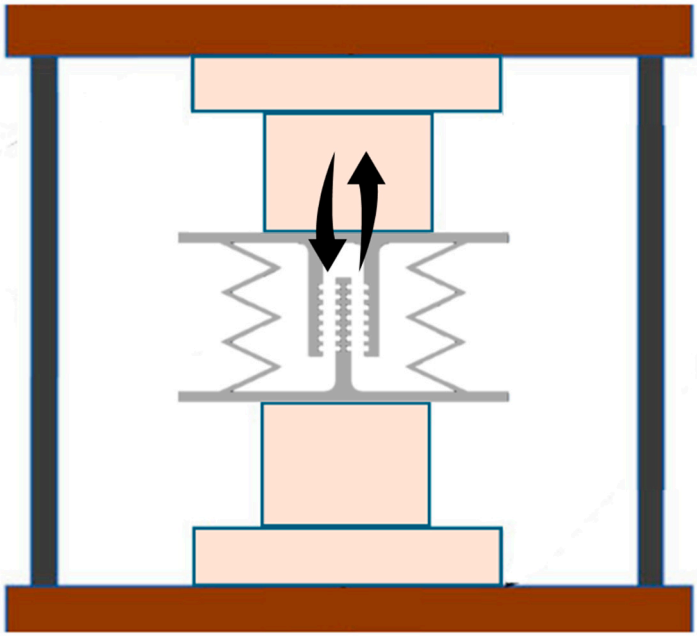

Figure 10. Prototype assembly diagram on the universal testing machine.

If a hysteresis loop is obtained, it indicates that there is dissipation of part of the energy. According to Rao [40], it is possible to relate this dissipated energy to the value of the damping coefficient. This relationship is given by Equation (23):

$$\Delta W = \oint F\,dx = \pi\omega c X^2 \tag{23}$$

In this equation, the dissipated energy, ΔW, and the damping, c, are unknown. This last parameter is the one you want to calculate, so you need to get the value of ΔW by another way. This was obtained through *Matlab*. To this end, the x and y vectors were introduced into the program, corresponding respectively to the displacement and load values. Next, the "polyarea" function was used, whose objective is to calculate the area within the curve of the graph. This procedure was adopted for all load–displacement datasets.

4. Results

4.1. Numerical Results

4.1.1. Ideal Stiffness and Damping

The *Matlab* code found the values of k = 13,422.66 N/m and c = 534.07 Ns/m, for a value of ξ = 0.25. It is also possible to verify that the transmissibility is lower than the unit from a frequency value of 2.87 Hz, and lower than the established value from 3.43 Hz. This represents, respectively, 88.5% and 86.3% of the defined frequency range. These values were calculated for a mass of 85 kg. The code can be adjusted in a simple way to calculate the values to k and c from other mass values. Figure 11 represents transmissibility as a function of excitation frequency, where the various curves represent the response of the system to various values of ξ.

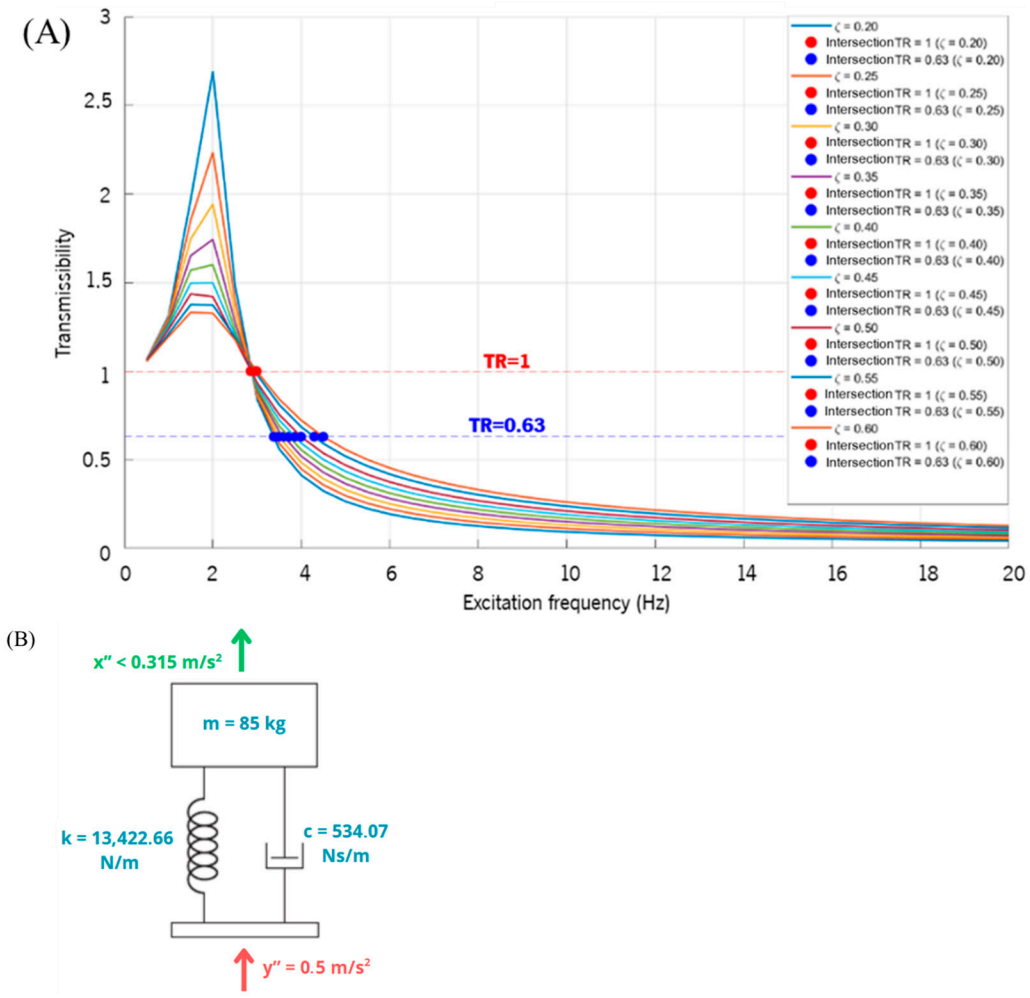

Figure 11. Transmissibility of the system as a function of the excitation frequency, (**A**) for various values of ξ, obtained from Matlab, and (**B**) representation of the equivalent system.

When compared to values reported in the literature, these results are in good agreement with typical human-centered vibration isolation systems and seat suspension models. For instance, Mandapuram et al. (2010) report transmissibility curves of similar shape, with isolation thresholds typically between 2 Hz and 4 Hz for damping ratios between 0.2 and 0.3 [69]. Similarly, Yand and Gong (2020) observed optimal damping ratios around 0.2–0.3 for minimizing acceleration transmissibility in low-frequency isolation systems [70]. The obtained parameters here thus fall within an optimal range that balances adequate damping without overly reducing the system's natural frequency.

Furthermore, the low transmissibility achieved beyond 3.5 Hz suggests that the system can efficiently protect the 85 kg mass (representing, for instance, a seated human or sensitive equipment) from base excitations of 0.5 m/s^2 amplitude. The results confirm that the Matlab implementation correctly captures the dynamic response predicted by analytical vibration theory and can be easily adapted for other mass configurations or damping scenarios.

4.1.2. Stiffness Element Analysis

The results obtained in the static analysis of the spring are presented below in Figure 12.

A displacement in the vertical direction of 0.076 mm (with a proof load of 20 N) and stress of 22.352 MPa (with a load of 850 N) were obtained.

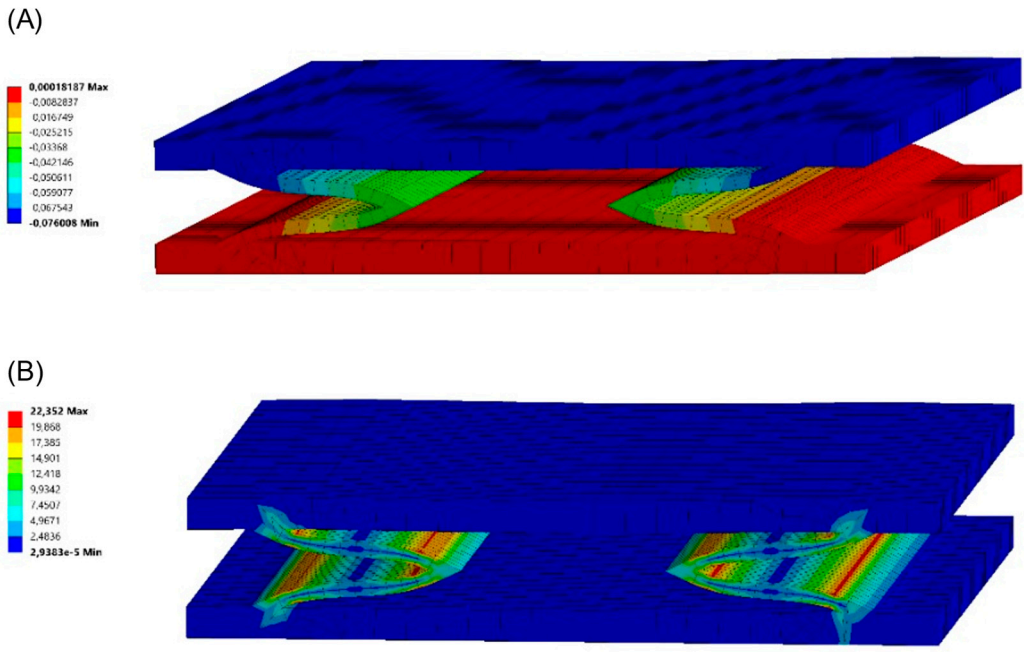

Figure 12. (**A**) Strain and (**B**) stress obtained in the structure for the base dimensions.

These values indicate a relatively stiff yet mechanically robust metamaterial structure. When compared with reported results in the literature, the obtained stiffness is at the higher end of typical values for locally resonant metamaterial unit cells, which commonly range between 10^3 N/m and 10^5 N/m, depending on the target resonant frequency and cell geometry [59,60]. For instance, a meta-plate design with a resonator stiffness of 9.59×10^4 N/m and an attached mass of 0.027 kg yielded resonant frequencies near 1 kHz [71–73], while designs aimed at lower-frequency bandgaps (tens to hundreds of hertz) typically employ spring constants below 10^4 N/m [74]. The simulated maximum von Mises stress of 22 MPa falls within the moderate range reported for similar metallic or composite metamaterial lattices, which typically show localized stress peaks between 5 MPa and 250 MPa depending on geometry and relative density [63,64]. These findings confirm that the proposed metamaterial architecture maintains structural integrity under operational loading while offering the potential for tailored dynamic responses through further geometric optimization.

Table 3 displays the optimal dimensions of the blade, taking into account the values of stiffness, installed stress, and number of blades. These dimensions, together with an extrusion depth of 200 mm, are ideal because the installed stress represents a safety coefficient of 1.77 (acceptable), and, considering the unit stiffness, 21 cells assembled in series are required to obtain adequate stiffness. Now, as each cell has a height of 24 mm, the total height of the structure will be 576 mm (without considering the tops and bases of the cells), a value leading to the common height of a public transport seat.

Table 3. Optimal dimensions of the blade supporting the parameterization of the new modeled structure.

Length (m)	Thickness (m)	Height (m)	Load (N)	Displacement (mm)	Stiffness (N/m)	Number of Cells	Max Stress (MPa)
0.0306	0.0053525	0.024	20	0.07099	281,722.09	20.99	21.66

4.1.3. Analysis of the Undamped Structure

With the data obtained for the 23 structures, Figure 13 was built to compare the stiffness obtained in the simulations with the expected theoretical stiffness values. Trend lines were obtained for each of the cases. It is possible to notice that there is some variation between the values of the computational tests in the analytical calculation; however, both of the obtained equations present excellent correlation values.

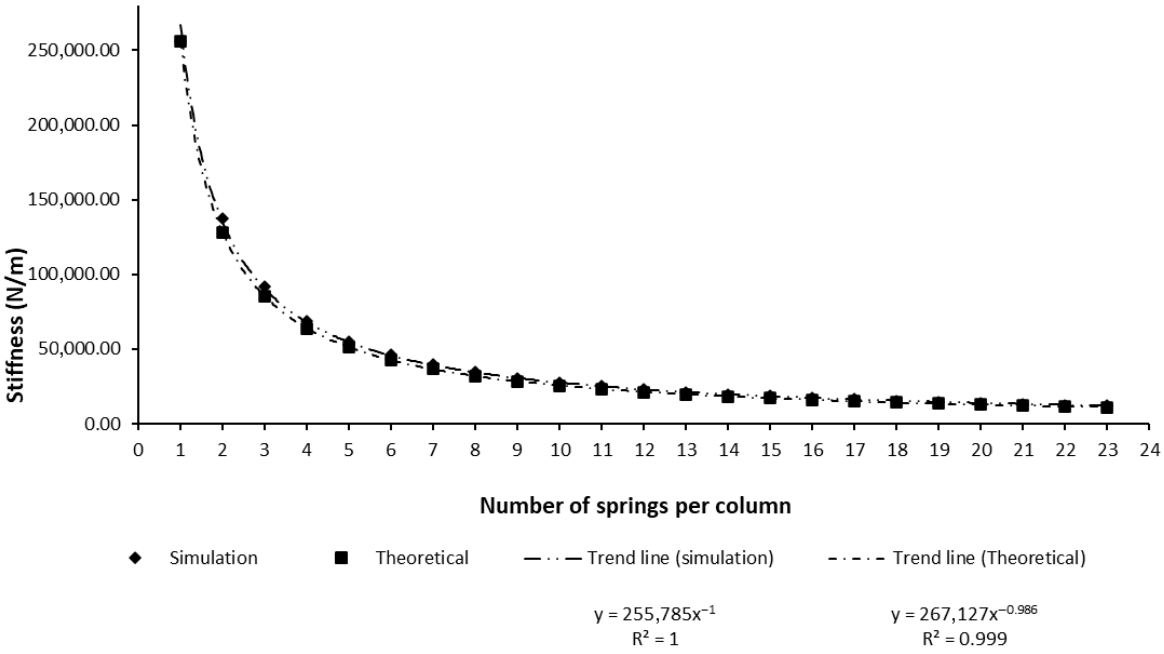

Figure 13. Simulation and theoretical stiffness curves of structures.

This data makes it possible to parameterize the structure, in the sense that it is possible to calculate the number of cells needed for stiffness values that are intended to be obtained for various applications, and vice versa. In order to simplify manufacturing and reduce the height of the structure, three blades were included for each column of each cell. Thus, it is possible to manufacture only seven cells, instead of 21 (where each of them would have only one blade per column). These data were also defined, taking into account a buckling analysis.

With the strain and stress values present in Figure 14, the values obtained for the stiffness (calculated according to the equation) and for the safety factor are 13,133.7 N/m and 1.94, respectively. In the buckling test, the first mode was found for a load value 2.47 times higher than the one that was imposed. The first vibration mode has a frequency of 1.96 Hz, a value very close to that calculated by the *Matlab* code (2 Hz). This slight difference is due to the fact that the stiffness obtained for the structure is slightly lower than that estimated by the code.

The graph of the amplitude of acceleration on the y-axis was obtained in the harmonic response test, and is presented in Figure 15. The resonance frequency occurs at 1.97 Hz, and the transmissibilities of 1 and 0.63 occur respectively at 2.8 and 3.195 Hz. The value of the acceleration at the peak resonance is 88.554 m/s^2, a very high value due to the lack of damping. However, the frequencies obtained are in line with what was obtained in the first simulation in *Matlab*.

The evaluation of the results focused on harmonic response graphs, which relate the acceleration felt at the top of the structure as a function of frequency. Four main pieces of information were extracted from them: the resonance frequency, the value of the acceleration in the resonance, and the frequencies at which transmissibility equals the

values of 1 and 0.63. By way of example, as noted in Figure 16, we have the graph obtained from the simulation of the 16 mm structure, cn1.

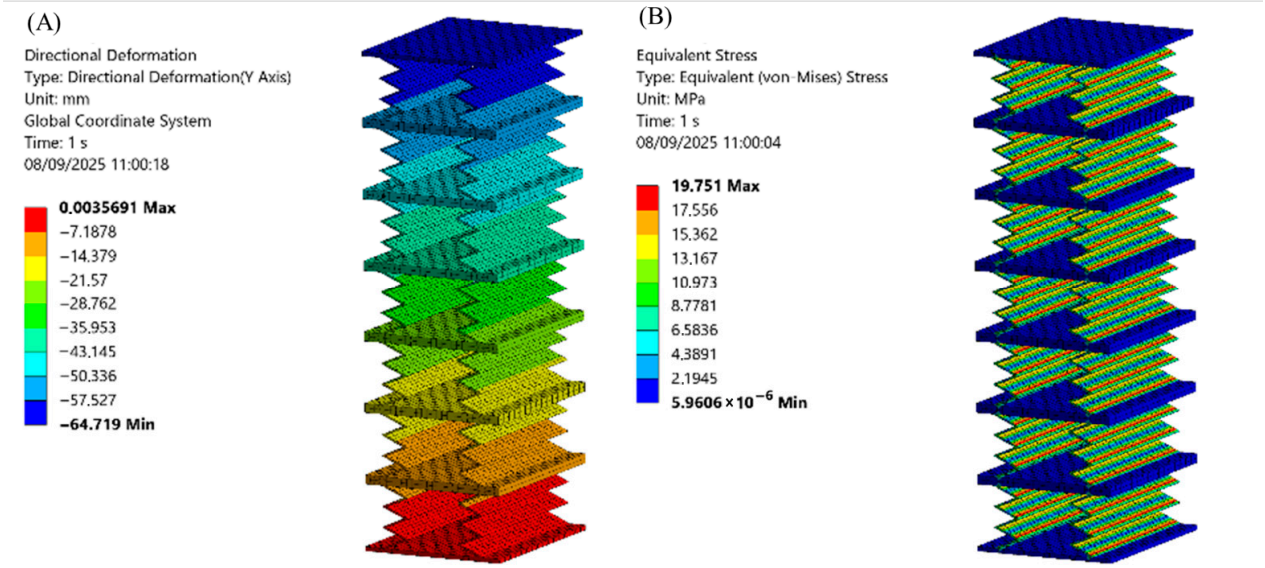

Figure 14. Static validation of the structure.

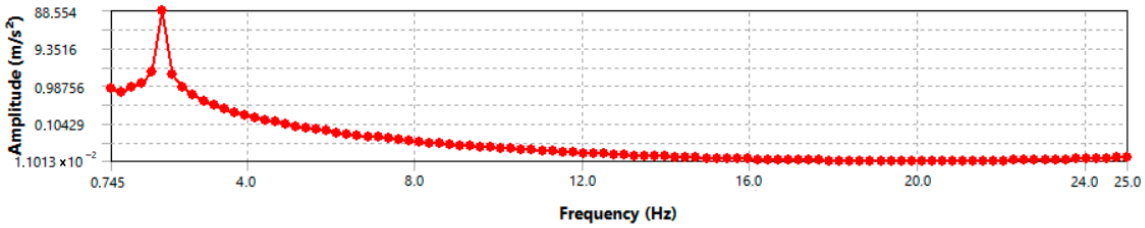

Figure 15. Acceleration amplitude of response in acceleration as a function of frequency in the harmonic analysis.

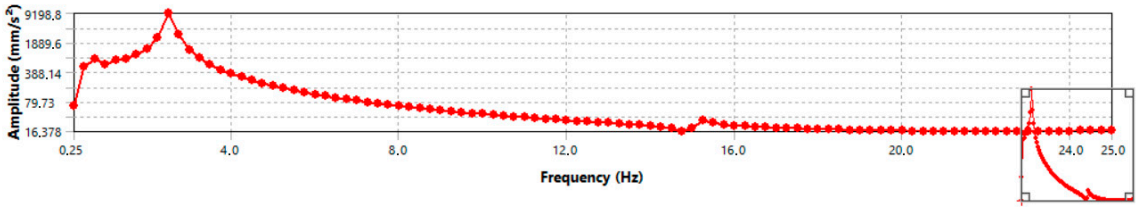

Figure 16. Acceleration amplitude as a function of frequency of the 16 mm-cn1 structure.

In this particular case, the resonance frequency value is 2.5 Hz, with an amplitude of 9.1988 m/s^2. Transmissibility values of 1 and 0.63 were reached, respectively, at 3.75 and 4.25 Hz. All the graphs obtained present the amplitude and phase angle curves with a shape similar to the presented case, and they meet the shape of the typical transmissibility graph, which ensures that the structure is assuming a behavior typical of an excited base structure. Only the graph representing the frequencies where transmissibility reaches the value of 0.63 (Figure 17) is presented in this work.

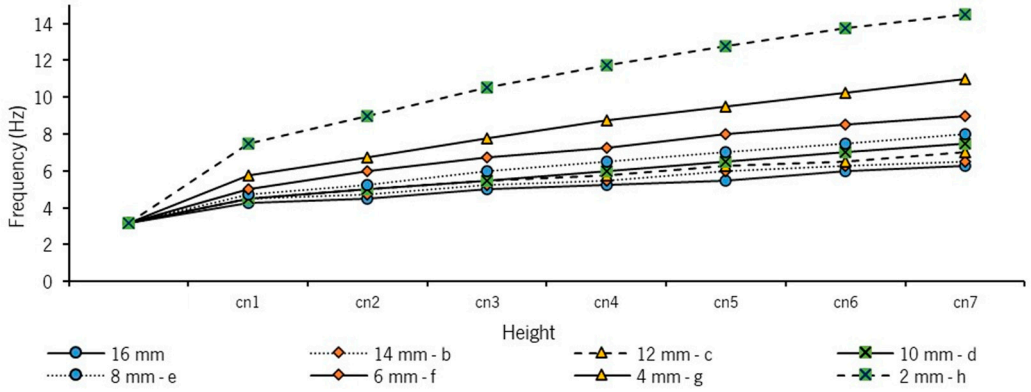

Figure 17. Variation in the frequency where T = 0.63, with the height of the structures for different widths.

It is possible to verify that the frequency where T = 0.63 of the structures increases as the width of the silicone decreases, and also to verify that there is a greater number of filled teeth. This can be explained by the increased stiffness provided by the silicone itself, i.e., its resistance to shear movement is increased with a smaller layer thickness and a higher height. Now, as there is an increase in the stiffness of the entire structure, according to Equation (4), the natural frequency of the structure will be higher, and therefore, the point where T = 1 will be higher, since the frequency values at that point are $\sqrt{2}$ times higher than the value of the natural frequency. Since the point where T = 1 moves to the right on the x-axis, the point where T = 0.63 will also be forced to move in the same direction, which justifies the relationship between this point and the natural frequency.

As far as the amplitude of acceleration in resonance is concerned, there is no standard to which all curves obey. As can be seen below in Figure 18, for lower heights of the silicon layer, the best results (lower acceleration values) can be found in the structures with smaller widths. However, as the height increases, these structures begin to show higher acceleration values. Structures with widths of 4 and 6 mm are those that present the best results for the entire range of heights analyzed. On the other hand, the cn5 and cn6 structures are those in which the acceleration value is the lowest for all widths. As a rule, very wide and low structures have high acceleration values, since they behave almost like a beam in flexion, and not like a structure when in shear, and therefore, they lose their dissipative capacity; on the other hand, thin and tall structures are too wide for shear movement to occur in the layer, and therefore, their behavior is more rigid, which again leads to higher acceleration peaks. The lowest values will be found in the balance between these two cases.

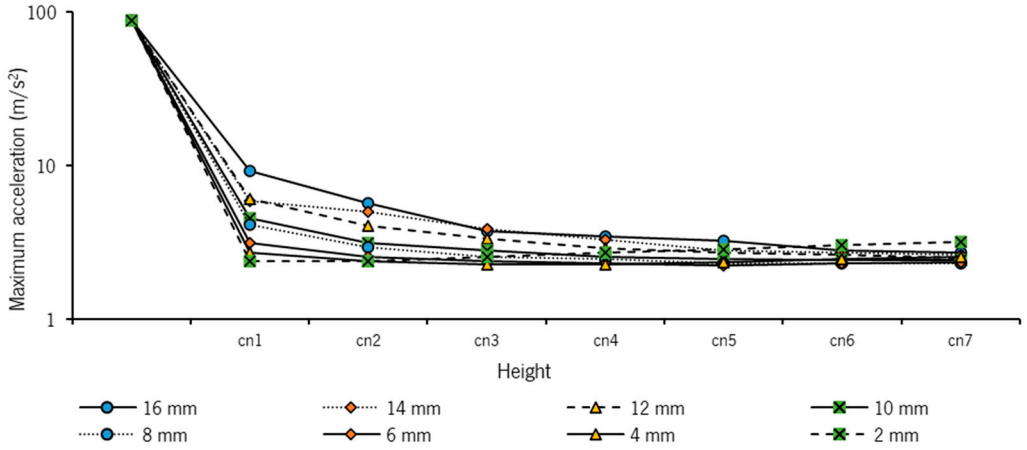

Figure 18. Variation in maximum acceleration with the width of the structures.

4.2. Experimental Results

4.2.1. Dynamic Mechanical Analysis Results

Figure 19 was obtained in the DMA test and has four curves of each of the moduli (storage and loss) as a function of temperature, with each of the curves corresponding to the various frequencies indicated above. The moduli values for the lower temperatures can be consulted in Appendix A.3, Table A3. The next step was to perform a curve fitting in the *Matlab*, with the data obtained in the DMA test, through the tool "cftool" to find the parameters of the Prony series, i.e., shear modulus at infinity, G_e, the relaxation modulus, G_i, and the relaxation time, τ_i. The values (Table 4), obtained with a correlation of $R^2 = 0.97771$, are further described in the discussion section below.

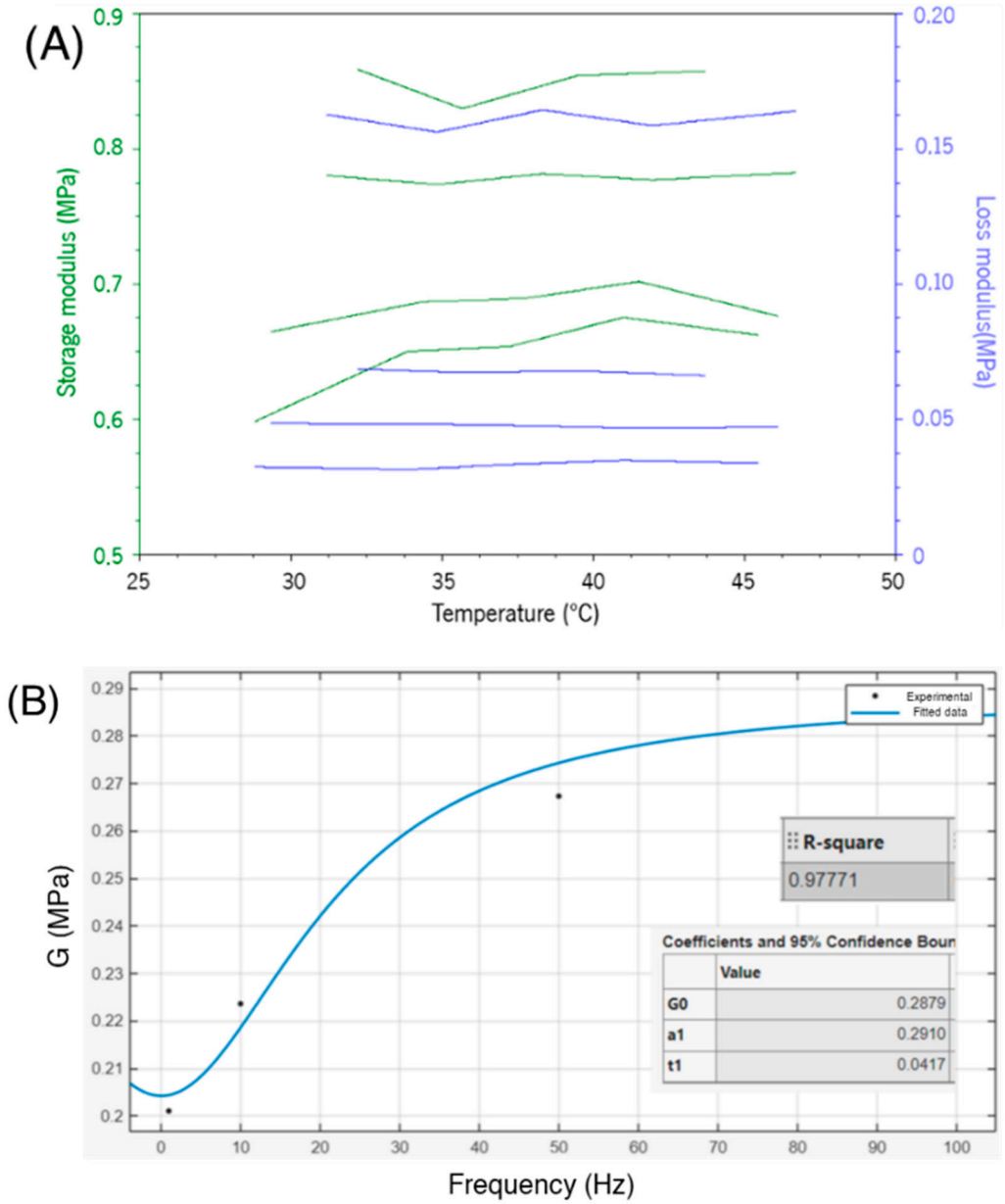

Figure 19. (**A**) Temperature–modulus curves for various frequencies, from the DMA test, and (**B**) regression of the Prony series in Matlab.

Table 4. Data from the Prony series of silicon obtained from *Matlab*.

Parameter	G_e [MPa]	G_i [MPa]	τ_i
Value	0.2879	0.2910	0.0417

The specific mass and the Poisson ratio also need to be defined in *Ansys*. The first parameter was calculated with the mass and volume of the sample produced, and the second was defined by taking into account some previous work [13] where this material has already been used. The data are summarized in Table 5.

Table 5. Silicon parameters defined in *Ansys*.

Parameter	Specific Mass [kg/m^3]	Poisson Ratio	G_e [MPa]	g_i	τ_i
Value	1144.78	0.49	0.2879	0.5027	0.0417

4.2.2. Experimental Harmonic Analysis

For each of the tests performed in the experimental test, a table of points was obtained with various information: load, instant, displacement, stress, and strain. For all these tests, a load–displacement curve was elaborated, as presented in Figure 20.

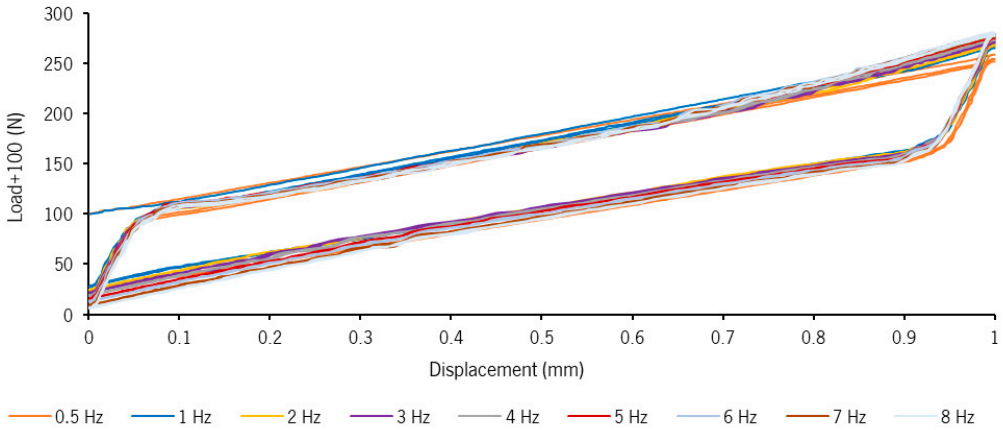

Figure 20. Load–displacement graph for the various frequencies.

All values of ΔW were recorded, and with Equation (23), the values of the damping coefficient were calculated, considering the amplitude value of 1 mm. Table 6 summarizes the values obtained in this process.

Table 6. Values of, and obtained for, ΔW and c in each of the experimental tests at different frequencies.

Frequency (Hz)	ω (rad/s)	ΔW (J)	c (Ns/m)
0.5	3.141593	0.1347	13,647.963
1	6.283185	0.201	10,182.779
2	12.566371	0.1836	4650.642
3	18.849556	0.1856	3134.202
4	25.132741	0.1937	2453.239
5	31.415927	0.2054	2081.137
6	37.699112	0.2122	1791.696
7	43.982297	0.2168	1569.031
8	50.265482	0.2202	1394.433

In order to corroborate the data obtained in the experimental test, a transient structural simulation was made, in which the pre-processing was carried out under loading conditions

and supports equal to those of the experimental tests. In each of them, only the set of points corresponding to the imposed displacement and the duration of the test were varied: these data were taken from the information that the test machine calculated for each of the tests. With regard to constraints, a fixed support at the base of the piece was defined; the imposed displacement was defined on the upper face in a tabular manner, according to the data of the experimental trials. The viscoelastic effect—through the Prony series—of ABS was also considered. The data were collected from a study by Ibrulj, Dzaferovic, Obucina and Kuzman [50], and are described in Appendix A.4, Table A4.

The post-processing consisted of obtaining the value of the force reaction and the displacement in the y-direction from the simulation. With this data, the load–displacement graphs were constructed, as with the experimental data. From this information, the values of ΔW and c were again calculated using the "polyarea" function and Equation (23). With this data, Table 7 was built.

Table 7. Values of ΔW and c obtained for each of the simulations at different frequencies.

Frequency (Hz)	Frequency (rad/s)	ΔW (J)	c (Ns/m)
0.5	3.141593	0.0276	2796.465
1	6.283185	0.0492	2492.501
2	12.566371	0.0789	1998.560
3	18.849556	0.0903	1524.884
4	25.132741	0.0907	1148.729
5	31.415927	0.0857	868.323
6	37.699112	0.0859	725.291
7	43.982297	0.0858	620.954
8	50.265482	0.0856	542.068

It is possible to see that the damping values obtained are lower than those obtained in the practical test. However, the evolution of both parameters is similar: in both tests, the values of the damping constant decrease as the test frequency increases. This phenomenon leads to the conclusion that the simulation does not represent the full damping capacity of the structure and/or silicone rubber in particular. This leads us to believe that the dissipative capabilities of silicone will not be fully represented in the simulations, which may be essentially related to the DMA tests carried out. These tests were carried out at the frequencies of 1, 10, 50, and 100 Hz, so that only two of these frequencies are included in the frequency range under study.

The stiffness of the structure was also calculated. This was made from the data from the lowest frequency test (0.5 Hz), particularly the data corresponding to the first charging cycle. Thus, the graph present on Appendix A.5, Figure A1, was prepared, and from this data, a linear trend line was created for this set of points. The slope of this line represents the stiffness of the structure. The obtained value for stiffness was 146.14 N/mm with an R^2 value of 0.9949, which indicates a good correlation between the data and the equation. This stiffness value corresponds to only one cell, so to obtain the total stiffness of the structure, this value should be divided by seven (seven cells in series), with $k_{Total} = 20,877.1$ N/m.

5. Discussion

5.1. Improvements in Vibration Transmission

According to the results obtained in the simulations, the developed structures can effectively reduce the acceleration that is applied to the base of the structure. Their design was made by considering the reduction in the transmissibility of vibrations, and for that, it was necessary to operate at a frequency $\sqrt{2}$ times higher than the natural frequency of the

structure. The great difficulty was to be able to work in this zone for low frequency values, as is the case here.

According to the harmonic response analysis carried out on the undamped structure, it can attenuate vibrations from 2.8 Hz; that is, it is at this value where the transmissibility is unitary. Considering the stiffness value of 13,422.66 N/m and the applied mass of 85 kg, $f_{T=1} = 2.83$ Hz. In other words, from this value, the structure fulfills one of the objectives for which it was designed. The objective was also set to reduce transmissibility to values below 0.63. Considering the input acceleration of 0.5 m/s^2, this will lead to an output value of 0.315 m/s^2, which is the limit value that the standard defines as comfortable. The frequency at which this goal is achieved is 3.195 Hz, so the structure will provide comfort from this value. The major problem associated with this structure is the fact that, due to the lack of damping, the acceleration at the resonance peak is excessively high (88.554 m/s^2), which means that the value of ξ is zero. This acceleration value could, in practice, cause the structure's disintegration. Therefore, the structure without damping can be used, but in situations where frequencies are always higher than the resonance.

Silicone was then introduced to reduce the resonance peak, to try to make a possible structure that could be used in the entire range of frequencies, including resonance; note that, in ISO 2631, only accelerations greater than 2 m/s^2 are cataloged as extremely uncomfortable; even so, it is possible to work with higher values in this region, as long as it is transitory, as the exposure time is also taken into account in the evaluation of comfort. The cn5–6 mm structure was the one where the acceleration at the lowest resonance was obtained: 2.2341 m/s^2 at a frequency of 4.5 Hz. This value, although included in the "extreme discomfort" region, according to the ISO 2631 standard, allows the structure to be used in applications that transiently cross that frequency, unlike the structure without damping, which, in the case of resonance, could collapse. The introduction of silicone into the structure leads to an increase in natural frequency due to the introduction of additional stiffness from that material. The unit transmissibility of this structure is achieved at a frequency of 7 Hz, and at 8 Hz, the value of 0.63 of that parameter is obtained. This structure will only provide comfort at frequencies higher than the first, but can be used in the region to the left of $\sqrt{2}$ times the natural frequency point.

The structures with damping, where a greater range of frequencies can be obtained with the values within the established target are cn1–16 mm, cn1–14 mm, and cn1–10 mm. These structures have resonance frequencies of 2.5 Hz, and the accelerations at these points reach the values of 9.1988, 5.8894, and 4.5576 m/s^2. Transmissibility below 1 is achieved at 3.75, 4 and 3.75 Hz, respectively, and less than 0.63 at 4.25 Hz for the first case and 4.5 Hz for the following ones. Again, these structures can be used at all frequencies, particularly cn1–10 mm. Although the acceleration falls into the "extremely uncomfortable" region, it can be used transiently in this region, and from 4.5 Hz, it is possible to obtain a feeling of comfort. However, its use in the resonance should be avoided, as the acceleration values are higher.

Although the structure CN5–6 mm exhibits a peak acceleration of 2.23 m/s^2 at resonance (4.5 Hz), this response occurs within a narrow frequency band around resonance; outside this region, the structure significantly reduces vibration transmissibility, achieving comfort-level accelerations above 8 Hz, which corresponds to the dominant excitation range in typical bus operation. Nevertheless, this resonance peak exceeds the ISO 2631 comfort threshold and highlights the need for further investigation focused on resonance mitigation strategies, such as increased damping, multi-stage or graded cellular architectures, or hybrid passive–adaptive solutions to broaden the comfort range and reduce peak response. Future work should explicitly investigate the influence of varying passenger loads

(empty to fully loaded conditions) on the dynamic response and optimal design parameters, enabling a more comprehensive assessment of real-world operational scenarios.

Using the developed *Matlab* code, an attempt was made to calculate the value of ξ of these structures, and from this, an estimate of the value of the damping constant c. The plot of the parameter curves was adjusted to values of ξ between 0.01 and 0.1, in increments of 0.01, as shown in Figure 21. Considering the lowest resonance acceleration value obtained in the developed structures (obtained in the cn5–6 mm structure, of 2.2341 m/s^2), and according to Equation (2), a transmissibility value of 4.4682 is obtained. The curve where $\xi = 0.1$ has the highest transmissibility value of 4.41283, which is the closest value to the one calculated for the structure.

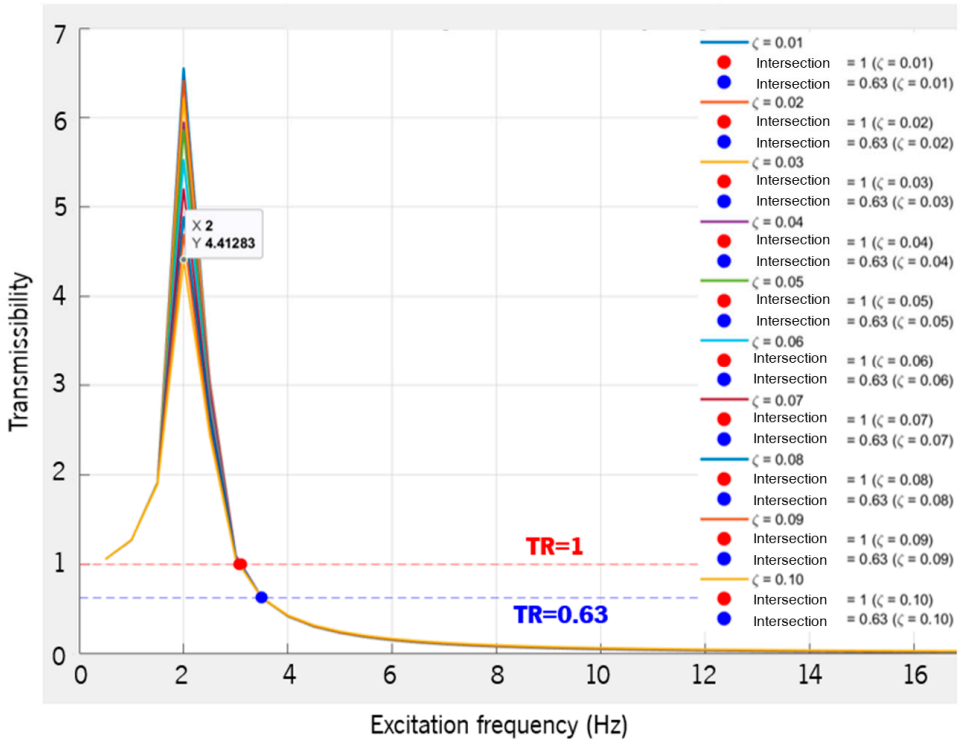

Figure 21. Transmissibility as a function of excitation frequency for various values of ξ.

According to Equation (6), the obtained damping coefficient for a single cell is $c = 480.664$ Ns/m. However, this damping value is slightly lower than that estimated by the *Matlab* code–534.07 Ns/m (this value was the one provided for the natural frequency of 2 Hz). Since this value represents the damping of the entire structure, consisting of seven cells in series, the damping of a unit made up of seven cells is $c_{unit} = 3364.65$ Ns/m.

The damping coefficients obtained experimentally showed a consistent decay with increasing excitation frequency. This behavior is characteristic of viscoelastic materials, whose energy dissipation capacity decreases with frequency due to reduced molecular mobility. The simulation results followed the same trend, though with values approximately one order of magnitude lower, indicating that the numerical model underestimates the dissipative behavior of the silicone–ABS system. Similar discrepancies have been reported in the literature, where the damping predicted by Prony-based models was found to be 3–10 times lower than experimental results due to the limitations of linear viscoelastic characterization within narrow frequency bands [75–77]. The experimental damping values obtained here are within the same order of magnitude as those reported for polymeric damping layers in vehicle applications (typically 10^3–10^4 Ns/m [67,68]), suggesting that the proposed metamaterial unit cell provides an adequate damping performance for vibration mitigation. The measured stiffness also falls within the range suitable for seat or support

systems in buses and trains, balancing compliance and energy dissipation. Overall, the results indicate that, despite the simulation underestimating the damping magnitude, the experimental behavior confirms the potential of the designed metamaterial to achieve industry-relevant dynamic comfort through passive damping mechanisms.

Although the simulations verified the incapacity of the silicon rubber to attenuate the resonance peak, the developed structure model makes a significant contribution to reducing transmissibility and increasing the associated dynamic comfort. The structure will have its efficiency for frequencies from 4 Hz. Now, most of the bibliographic references consulted indicate that the critical frequencies start in this range: frequencies that affect the lumbar region are between 4 and 10 Hz; frequencies that affect the chest and abdominal area are between 5 and 10 Hz; and frequencies that affect the head and neck are between 20 and 30 Hz. In other words, the developed structure manages to attenuate this frequency range and bring the acceleration value to the level that the standard defines as "comfortable"—below 0.315 m/s^2. Within the spectrum of values between 0 and 25 Hz, the range defined for this problem, the developed structure is able to provide comfort in about 84% of this range, as can be seen in Figure 22.

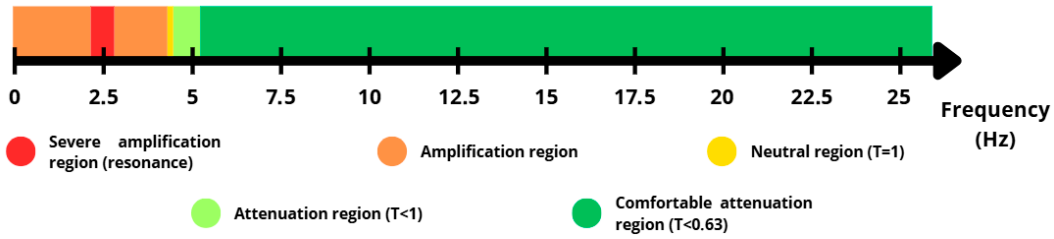

Figure 22. General behavior of the structure in relation to transmissibility over frequency.

Since it was not possible to reduce the resonance peak in the way that was initially intended, further investigation needs to be conducted for the structure to be used in vehicles where frequencies in the order of 2–3 Hz are persistent. There is also great difficulty in attenuating low-frequency vibrations, as it is only possible to work in an attenuation zone at least $\sqrt{2}$ times higher than the natural frequency. The development of structures with low natural frequency requires very high mass and very low stiffness (cf. Equation (4)), which, in most cases, may cause mechanical resistance problems. Possible future solutions will include the use of materials and/or metamaterials with zero or even negative stiffness, or the use of active or semi-active systems that guarantee a more effective and regulated control of vibratory forces. It should be remembered that these systems represent higher costs, and metamaterials with QZS or HSLDS usually have complex geometries for manufacturing using conventional and easily industrialized manufacturing processes.

5.2. Industrial Feasibility

The development and production of metamaterials is mainly based on additive manufacturing methods. However, these options are not yet ready for series production, mainly due to the high production cycle times. Thus, the unit cell was designed with a capable geometry of being manufactured not only by additive manufacturing, but also by so-called traditional processes, such as polymer injection. Thus, the profile of the unit cell allows it to be injected in a direction perpendicular to the plane on this page, as well as to manufacture it without the addition of cores and to release it without additional difficulties.

The molds used in this process have a wide variety of dimensions, and may, if they have a cubic geometry, vary between 200 and 1000 mm on a side. This could allow multiple cells to be manufactured in the same mold. The maximum recommended thickness for manufacturing is 5 mm, so that there is a good filling of the mold. The unit cell has regions

where the thickness is equal to this value, and it is higher in some regions; however, these areas are not critical, and their thickness may be reduced. The only thickness that influences the stiffness values is that of the springs, which are around 2.25 mm. The wall thickness influences the timing of each injection cycle. Generally, the cycle time of this manufacturing process can take, on average, between 20 and 200 s, from the moment the mold is closed for the start of the injection until it is opened for the expulsion of the injected part(s). This variable depends on several factors, such as the material used and the temperatures, pressures, thickness, and quantity of the parts. Note that, for this particular case, an ABS part with an overall thickness of 5 mm has a cooling time of 44.4 s, and is manufactured in a water-cooled mold [78–80]. However, the duration of the cooling period represents about 64% of the entire injection cycle, according to Selvaraj, Raj, Mahadevan, Chadha, and Paramasivan [81]. In this way, it is possible to estimate the production time of a unit cell at about 69.4 s. Figure 23 represents the percentage division of the stages of the injection process, according to these authors.

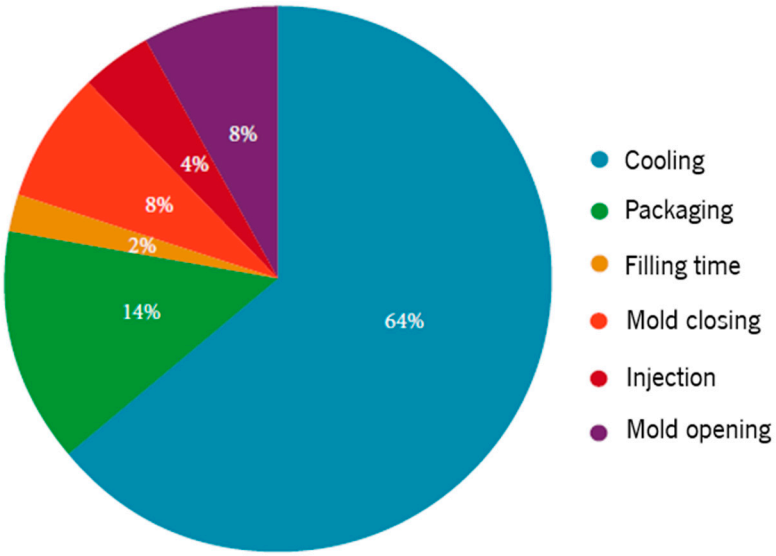

Figure 23. Percentage division of injection process steps (adapted) [78].

The number of cells produced will also depend on the size of the mold, i.e., whether it allows the manufacture of one or several cells simultaneously. Consider, for example, a mold with the capacity to produce three cells simultaneously. Thus, per hour, the number of cells produced is given by:

$$Nr.cell/hour = \frac{1\text{ h}}{69.4\text{ s}} \times 3 = \frac{3600\text{ s}}{69.4\text{ s}} \times 3 \approx 156 \quad (24)$$

As already mentioned, the structure consists of seven cells. Considering the number of cells produced per hour calculated in Equation (24), the number of structures that can be obtained in the same period is given by:

$$Nr.strutures/hour = \frac{156}{7} = 22.3 \quad (25)$$

Of course, the times for placing the silicone or assembling the cells are not being considered. The connection between them can be ensured by bolted connections, as they are simple, low-cost, and maintenance-free. This allows us to maintain the simplicity and low cost of the entire product. The introduction of silicone is a relatively simple process. It is only necessary to make the respective seals so that it fills the desired cavity.

According to a supplier of various polymers, the price of ABS is approximately €2.19/kg. The mass of the prototype manufactured is 270 g, but its thickness was about 50% of the value that was sought. The projected structure, with the seven units, has a value of €8.28. The value of the silicone and catalyst used, reference AE SC 23, was estimated at 34.30 €/kg. Using, once again, the manufactured prototype, the silicone mass used was 57.99 g. A complete body, therefore, requires 811.86 g, which leads to a total value of €27.85. Adding this value to that of ABS, a total of €36.13 in raw material expenses is obtained.

The price of double seats on city buses is around 30 €/unit. Disregarding the price of the current supports—which, in principle, would be a small fraction of the price of the seat, given that they are only extruded aluminum or steel profiles—the price of a double seat could amount to around 100 €, considering the sum between the current value of this product and the estimated value in the production of two support structures. The solution developed, despite increasing the cost compared to existing solutions, is an important step in increasing passenger comfort in public transport. The increase is practically negligible when compared with the total cost of a vehicle with and without this solution. Consider, as an example, the City Gold model from Caetanobus/Toyota, introduced to the market in 2020. This vehicle was launched with a price of approximately 425,000 €, and has 34 seats, so this will be the number of vibration attenuating structures to be used, which is in addition to the initial value 1224 €. Now, this represents only 0.29% of the initial cost of the bus, so it is an insignificant addition that can make the vehicles more comfortable and appealing. The solution presented aims to introduce comfort while conserving the total cost of the vehicle. Of course, a suspension system similar to those used in drivers' seats would be an excellent improvement in passenger comfort. However, these systems are usually active or semi-active systems (or passive with air suspension), and they are developed together with the entire seat structure, and so, due to their complexity, the price is much higher, standing between 500 € and 2000 € per seat, depending on the type of system.

6. Conclusions

For public transport to be inviting, it is necessary that it offers, among other things, conditions of comfort, particularly the physical ones, which are significantly influenced by the dynamic loads existing in vehicles. Passenger seats are normally rigidly attached to the body of the vehicle, so that all dynamic loads to which the chassis is subjected are transferred to the seats. In this work, the development of a concept that could solve this rigid assembly by a solution capable of reducing the transmissibility of vibrations to passengers, without introducing high costs and complexity, was explored. Note that a driver's seat is usually equipped with active vibration attenuation systems, but in this case, this application is justifiable, not only because it is only a single case, but also because the time of exposure to dynamic loads is much longer, which increases the risk of developing a series of diseases that have already been presented.

Thus, the solution sought was based on the concept of metamaterial, that is, a material that is designed to have certain properties. This type of solution results in simple systems with few components and thus leads to a reduction in production and maintenance costs. The structure was designed to have a certain stiffness and mechanical resistance, and damping given by an external material (silicone), which is easily included in the structure. Through this concept, various responses were achieved for the frequency range between 0 and 25 Hz, which vary mainly with the configuration of the silicone rubber. In general, it is possible to achieve a comfortable attenuation of vibrations from around 4/5 Hz, which is quite positive considering the problematic frequencies already identified. Now, the installation of these structures in bus and train seats could bring significant improvements in passenger comfort, which will make these forms of mobility more appealing to use.

Author Contributions: Conceptualization, T.C., N.A.T.C.F. and Ó.C.; methodology, T.C., D.S., N.A.T.C.F. and Ó.C.; software, T.C. and N.A.T.C.F.; validation, T.C., D.S., N.A.T.C.F. and Ó.C.; formal analysis, T.C.; investigation, T.C.; resources, Ó.C.; data curation, T.C. and N.A.T.C.F.; writing—original draft preparation, T.C.; writing—review and editing, T.C., D.S., N.A.T.C.F. and Ó.C.; visualization, T.C. and N.A.T.C.F.; supervision, N.A.T.C.F. and Ó.C.; project administration, Ó.C.; funding acquisition, Ó.C. All authors have read and agreed to the published version of the manuscript.

Funding: The authors gratefully acknowledge the funding by Ministério da Ciência, Tecnologia e Ensino Superior, FCT, Portugal, under national support to the R&D unit's grant through references UIDB/04436/2020 and UIDP/04436/2020, and under the individual PhD grants with references 2022.11063.BD. This study was supported by LABBELS–Associate Laboratory in Biotechnology, Bioengineering and Microelectromechanical Systems, LA/P/0029/2020. In addition, this work was under the project "BrainStimMap—Mapping and modeling the transmission profile of optomechanical waves in the brain to optimize transcranial stimulation against brain disorders" with the reference PTDC/EME-EME/1681/2021.

Institutional Review Board Statement: Not applicable.

Informed Consent Statement: Not applicable.

Data Availability Statement: The data presented in this study are available in the article.

Conflicts of Interest: The authors declare no conflicts of interest.

Abbreviations

The following abbreviations are used in this manuscript:

CLD	Constrained layer damping
DMA	Dynamic mechanical analysis
ABS	Acrylonitrile butadiene styrene
PLA	Polylactic acid
TPU	Thermoplastic polyurethane
WBV	Whole body vibration

Appendix A

Appendix A.1

Table A1. Applied displacement as a function of frequency for harmonic analysis.

Frequency (Hz)	Displacement (mm)
0	0
0.5	50.661
1	12.665
1.5	5.629
2	3.1663
2.5	2.0264
3	1.4072
3.5	1.0339
4	0.79157
4.5	0.62544
5	0.50661

Appendix A.2

Table A2. Prototype printing parameters.

Parameter	Value
Layer height	0.5 mm
Nozzle diameter	1 mm
Wall thickness	3 mm
Base adhesion geometry	Brim (5 outlines)
Infill	20%
Infill pattern	Grid
Base Temperature	100 °C
Extrusion Temperature	250 °C
Print speed	50 mm/s
Fan Speed	25%

Appendix A.3

Table A3. Summary Table of data obtained from the DMA test for silicon. * is part of the variable complex modulus.

Parameter	Storage Modulus E′ (MPa)	Storage Modulus G′ (MPa)	Loss Modulus E″ (MPa)	Loss Modulus G″ (MPa)	Complex Modulus G*
1	0.598	0.201	0.032	0.011	0.201
10	0.665	0.223	0.048	0.016	0.224
50	0.780	0.262	0.163	0.055	0.267
100	0.859	0.288	0.069	0.023	0.289

Appendix A.4

Table A4. Definition of ABS Prony series.

Index i	Relative Modulus	Relaxation Time	Temperature
1	0.11	0.33	20 °C
2	0.1	0.031	

Appendix A.5

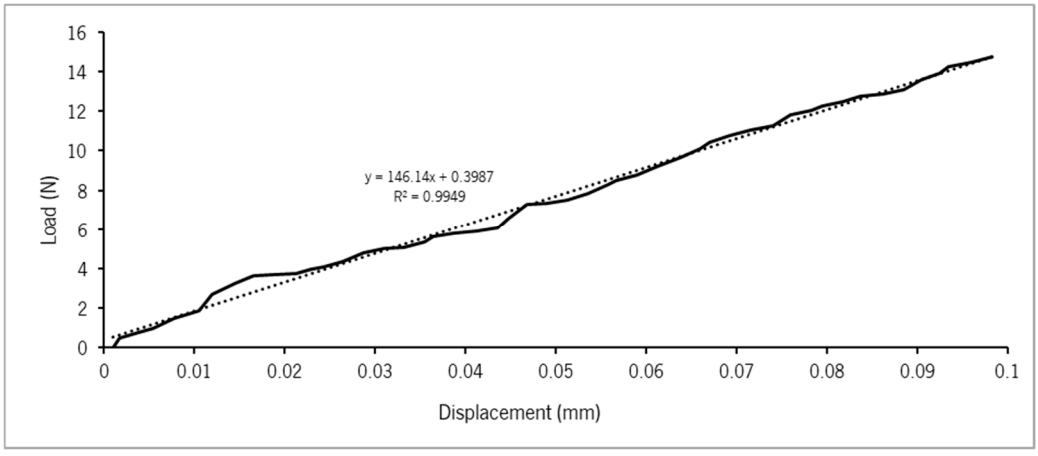

Figure A1. Load–displacement curve used for stiffness calculation.

References

1. Directorate-General for Communication Transport and Tourism. Available online: https://commission.europa.eu/topics/transport-and-tourism_en (accessed on 30 October 2025).
2. de Portugal, G. *Governo Anuncia 240 Milhões de Euros de Financiamento Para Transportes Públicos 2024*; XXV Governo Constitucional de Portugal: Lisbon, Portugal, 2024.
3. de Portugal, G. *Sustentável 2030: Programa Temático Para a Ação Climática e Sustentabilidade*; Ministério do Meio Ambiente e Mudança do Clima: Brasília, Brazil, 2023.
4. de Portugal, G. *Plano Nacional de Investimentos 2030*; Governo da República Portuguesa: Lisboa, Portugal, 2020.
5. Comission, E. *Green Paper: Towards a New Culture of Urban Mobility*; European Commission: Bruxels, Belgium, 2007.
6. Agência Europeia do. *Transport and Environment Report 2021: Decarbonising Road Transport—The Role of Vehicles, Fuels and Transport Demand*; Agência Europeia do Ambiente: Copenhagen, Denmark, 2022.
7. Chan, W.C.; Wan Ibrahim, W.H.; Lo, M.C.; Suaidi, M.K.; Ha, S.T. Determinants of Customer Satisfaction and Loyalty in Public Transport: A PLS-SEM Approach. *Stud. Appl. Econ.* **2021**, *39*, 3–23. [CrossRef]
8. Filipa Pinheiro Da Silva, P.; Mendes, J. Passengers Comfort Perception and Demands on Railway Vehicles: A Review. *KnE Eng.* **2020**, *2020*, 257–270. [CrossRef]
9. Bhiwapurkar, M.K.; Saran, V.H.; Harsha, S.P. Interference in Writing Performance under Whole-Body Vibration Exposure Together with Subject Posture. *Int. J. Veh. Noise Vib.* **2016**, *12*, 182. [CrossRef]
10. Khan, M.S.; Sundstrom, J. Effects of Vibration on Sedentary Activities in Passenger Trains. *J. Low Freq. Noise Vib. Act. Control* **2007**, *26*, 43–55. [CrossRef]
11. Fernandes, N.A.T.C.; Arieira, A.; Hinckel, B.; Silva, F.; Leal, A.; Carvalho, Ó. A Python FDTD Method Algorithm for 1D Planar Acoustic Wave Propagation: Simulating High-Frequency Ultrasound in the Brain and Beyond. In *Proceedings of ICOVP and WMVC 2025; Mechanisms and Machine Science*; Dimitrovová, Z., Biswas, P., Silva, T.A.N., Eds.; Springer Nature: Cham, Switzerland, 2026; Volume 197, pp. 391–401. ISBN 978-3-032-13224-6.
12. Sharma, S.; Fernandes, N.A.T.C.; Carvalho, Ó. A Frequency-Dependent and Nonlinear, Time-Explicit Five-Layer Human Head Numerical Model for Realistic Estimation of Focused Acoustic Transmission Through the Human Skull for Noninvasive High-Intensity and High-Frequency Transcranial Ultrasound Stimulation: An Application to Neurological and Psychiatric Disorders. *Bioengineering* **2025**, *12*, 1161. [CrossRef]
13. Fernandes, N.A.T.C.; Alves, D.I.; Ferreira, D.P.; Monteiro, M.; Arieira, A.; Silva, F.; Hinckel, B.; Leal, A.; Carvalho, Ó. Sustainable Tunable Anisotropic Ultrasound Medical Phantoms for Skin, Skeletal Muscle, and Other Fibrous Biological Tissues Using Natural Fibers and a Bio-Elastomeric Matrix. *J. Compos. Sci.* **2025**, *9*, 370. [CrossRef]
14. Santos, A.Z.; Rocha, S.; Fernandes, N.A.T.C.; Alves, D.I.; Ferreira, D.P.; Costa, S.M.; Padrão, J.; Carvalho, Ó. Sustainable Shear Wave Elastography Medical Phantoms: Waste-Based Fibrous Structures for Medical Applications. *Textiles* **2026**, *6*, 6. [CrossRef]
15. Santos, A.Z.; Rocha, S.; Carneiro, B.; Fernandes, N.A.; Padrão, J.; Carvalho, Ó. Current State of Elastography Research in Multiple Anatomical Structures and Respective Phantoms. *Phys. Medica* **2025**, *138*, 105192. [CrossRef]
16. Fernandes, N.A.T.C.; Sharma, S.; Arieira, A.; Hinckel, B.; Silva, F.; Leal, A.; Carvalho, Ó. Experimental Validation of Time-Explicit Ultrasound Propagation Models with Sound Diffusivity or Viscous Attenuation in Biological Tissues Using COMSOL Multiphysics. *Bioengineering* **2025**, *12*, 946. [CrossRef] [PubMed]
17. Fernandes, N.; Silva, F.S.; Carvalho, Ó.; Leal, A. The Effect That Lower Limb Orthoses Have on Cartilage on Patients with Knee Osteoarthritis: A Narrative Review. *Prosthet. Orthot. Int.* **2022**, *47*, 466–476. [CrossRef] [PubMed]
18. European Commission. *Directorate-General for Employment, Social Affaires and Equal Opportunities Non-Binding Guide to Good Practice with a View to Implementation of Directive 2002/44/EC on the Minimum Health and Safety Requirements Regarding the Exposure of Workers to the Risks Arising from Physical Agents (Vibrations)*; Publications Office: Luxembourg, 2008.
19. *ISO 2631*; Mechanical Vibration and Shock—Evaluation of Human Exposure to Whole-Body Vibration. ISO: Geneve, Switzerland, 1997.
20. Fedatto Neto, M.; Gomes, H.M. Análise de Níveis de Vibração Em Usuários de Trens Urbanos. *Estud. Tecnológicos Eng.* **2018**, *12*, 24–44. [CrossRef]
21. Zhao, Y.; Wang, X. A Review of Low-Frequency Active Vibration Control of Seat Suspension Systems. *Appl. Sci.* **2019**, *9*, 3326. [CrossRef]
22. Krajnak, K. Health Effects Associated with Occupational Exposure to Hand-Arm or Whole Body Vibration. *J. Toxicol. Environ. Health Part B* **2018**, *21*, 320–334. [CrossRef]
23. Zolfagharian, A.; Picken, P.; Bodaghi, M.; Fard, M.; Rolfe, B. Additive Manufacturing of Composite Foam Metamaterial Springs for Vibration Isolation. *Adv. Eng. Mater.* **2023**, *25*, 2300356. [CrossRef]
24. Zhang, C.; Kordestani, H.; Shadabfar, M. A Combined Review of Vibration Control Strategies for High-Speed Trains and Railway Infrastructures: Challenges and Solutions. *J. Low Freq. Noise Vib. Act. Control* **2023**, *42*, 272–291. [CrossRef]

25. Atindana, V.A.; Xu, X.; Nyedeb, A.N.; Quaisie, J.K.; Nkrumah, J.K.; Assam, S.P. The Evolution of Vehicle Pneumatic Vibration Isolation: A Systematic Review. *Shock Vib.* **2023**, *2023*, 1716615. [CrossRef]
26. Johnson, P.W.; Ibbotson-Brown, J.; Menocal, S.; Parison, J. Comparison of Whole-Body Vibration Exposures When Operating a City Bus with an Active, Passive and Static Suspension Bus Seat. *Proc. Hum. Factors Ergon. Soc. Annu. Meet.* **2019**, *63*, 1052–1056. [CrossRef]
27. Papaioannou, G.; Sekulic, D.; Velenis, E.; Antoniadis, I. *Investigation of Seat Suspensions with Embedded Negative Stiffness Elements for Isolating Bus Users' Whole-Body Vibrations*; SAE International: Warrendale, PA, USA, 2021; p. 2021-01-5019.
28. Yang, Y.; Liu, C.; Chen, L.; Zhang, X. Phase Deviation of Semi-Active Suspension Control and Its Compensation with Inertial Suspension. *Acta Mech. Sin.* **2024**, *40*, 523367. [CrossRef]
29. Suresh Kumar, N.; Naidu, K.C.B.; Banerjee, P.; Anil Babu, T.; Venkata Shiva Reddy, B. A Review on Metamaterials for Device Applications. *Crystals* **2021**, *11*, 518. [CrossRef]
30. Askari, M.; Hutchins, D.A.; Thomas, P.J.; Astolfi, L.; Watson, R.L.; Abdi, M.; Ricci, M.; Laureti, S.; Nie, L.; Freear, S.; et al. Additive Manufacturing of Metamaterials: A Review. *Addit. Manuf.* **2020**, *36*, 101562. [CrossRef]
31. Lakamanahalli, A.S.; Hudedmani, M.G.; Shweta, G.M.; Hoskeri, P.; Mathad, S.N. Metamaterials: A Comprehensive Review of Design and Applications. *Int. J. Adv. Sci. Eng.* **2024**, *11*, 3816–3835. [CrossRef]
32. Wang, H.; Lyu, Y.; Bosiakov, S.; Zhu, H.; Ren, Y. A Review on the Mechanical Metamaterials and Their Applications in the Field of Biomedical Engineering. *Front. Mater.* **2023**, *10*, 1273961. [CrossRef]
33. Wang, Z.; Luan, C.; Liao, G.; Liu, J.; Yao, X.; Fu, J. Progress in Auxetic Mechanical Metamaterials: Structures, Characteristics, Manufacturing Methods, and Applications. *Adv. Eng. Mater.* **2020**, *22*, 2000312. [CrossRef]
34. Yu, X.; Zhou, J.; Liang, H.; Jiang, Z.; Wu, L. Mechanical Metamaterials Associated with Stiffness, Rigidity and Compressibility: A Brief Review. *Prog. Mater. Sci.* **2018**, *94*, 114–173. [CrossRef]
35. Dalela, S.; Balaji, P.S.; Jena, D.P. A Review on Application of Mechanical Metamaterials for Vibration Control. *Mech. Adv. Mater. Struct.* **2022**, *29*, 3237–3262. [CrossRef]
36. Su, R.; Chen, J.; Zhang, X.; Wang, W.; Li, Y.; He, R.; Fang, D. 3D-Printed Micro/Nano-Scaled Mechanical Metamaterials: Fundamentals, Technologies, Progress, Applications, and Challenges. *Small* **2023**, *19*, 2206391. [CrossRef]
37. Fayyaz; Bashmal, S.; Nazir, A.; Khan, S.; Alofi, A. Damping Optimization and Energy Absorption of Mechanical Metamaterials for Enhanced Vibration Control Applications: A Critical Review. *Polymers* **2025**, *17*, 237. [CrossRef] [PubMed]
38. Al Rifaie, M.; Abdulhadi, H.; Mian, A. Advances in Mechanical Metamaterials for Vibration Isolation: A Review. *Adv. Mech. Eng.* **2022**, *14*, 16878132221082872. [CrossRef]
39. Hamzehei, R.; Bodaghi, M.; Wu, N. Mastering the Art of Designing Mechanical Metamaterials with Quasi-Zero Stiffness for Passive Vibration Isolation: A Review. *Smart Mater. Struct.* **2024**, *33*, 083001. [CrossRef]
40. Rao, S. *Mechanical Vibrations*, 6th ed.; Pearson: Upper Saddle River, NJ, USA, 2017.
41. Wang, H.; Lee, H.P.; Du, C. Analysis and Optimization of Damping Properties of Constrained Layer Damping Structures with Multilayers. *Shock Vib.* **2021**, *2021*, 6740696. [CrossRef]
42. Rao, M.D. Recent Applications of Viscoelastic Damping for Noise Control in Automobiles and Commercial Airplanes. *J. Sound Vib.* **2003**, *262*, 457–474. [CrossRef]
43. Merideno, I.; Nieto, J.; Gil-Negrete, N.; Landaberea, A.; Iartza, J. Constrained Layer Damper Modelling and Performance Evaluation for Eliminating Squeal Noise in Trams. *Shock Vib.* **2014**, *2014*, 473720. [CrossRef]
44. Xie, Z.; Steve Shepard, W. Development of a Single-Layer Finite Element and a Simplified Finite Element Modeling Approach for Constrained Layer Damped Structures. *Finite Elem. Anal. Des.* **2009**, *45*, 530–537. [CrossRef]
45. Shu, Z.; You, R.; Zhou, Y. Viscoelastic Materials for Structural Dampers: A Review. *Constr. Build. Mater.* **2022**, *342*, 127955. [CrossRef]
46. Zhou, J.; Yang, Z.; Feng, X.; Zhao, X. Dynamic Viscoelastic Analysis and Experiment of an Aerospace Silicone Rubber Damper Based on DMA Test. In Proceedings of the 2021 the 5th International Conference on Robotics, Control and Automation, Seoul, Republic of Korea, 5 March 2021; pp. 58–62.
47. Tapia Romero, M.A.; Dehonor Gomez, M.; Lugo Uribe, L.E. Prony Series Calculation for Viscoelastic Behavior Modeling of Structural Adhesives from DMA Data. *Ing. Investig. Y Tecnol.* **2020**, *21*, 1–10. [CrossRef]
48. *ISO 6721-1*; Plastics—Determination of Dynamic Mechanical Properties—Part 1: General Principles. ISO: Geneve, Switzerland, 2019.
49. Gallimore, C. Passive Viscoelastic Constrained Layer Damping Application for a Small Aircraft Landing Gear System. Master's Thesis, Virginia Polytechnic Institute and State University, Blacksburg, VA, USA, 2008.
50. Ibrulj, J.; Dzaferovic, E.; Obucina, M.; Kuzman, M.K. Numerical and Experimental Investigations of Polymer Viscoelastic Materials Obtained by 3D Printing. *Polymers* **2021**, *13*, 3276. [CrossRef]
51. Melo, R.M. *Exposição Ocupacional a Vibrações Transmitidas Ao Corpo Inteiro: Factores Condicionantes Na Condução de Autocarros Urbanos*; Universidade Técnica de Lisboa, Faculdade de Motricidade Humana: Lisboa, Portugal, 2006.

52. Paddan, G.S.; Griffin, M.J. Effect of Seating on Exposures to Whole-Body Vibration in Vehicles. *J. Sound Vib.* **2002**, *253*, 215–241. [CrossRef]
53. Paddan, G.S.; Griffin, M.J. Evaluation of Whole-Body Vibration in Vehicles. *J. Sound Vib.* **2002**, *253*, 195–213. [CrossRef]
54. Susatio, Y.; Oktaviana, L.; Rizki, N.K.; Listijorini, E.; Biyanto, T.R. Design of Half-Car Active Suspension System for Passenger Riding Comfort. *J. Phys. Conf. Ser.* **2018**, *1075*, 012030. [CrossRef]
55. Calvo, J.A.; Diaz, V.; Roman, J.L.S. Establishing Inspection Criteria to Verify the Dynamic Behaviour of the Vehicle Suspension System by a Platform Vibrating Test Bench. *Int. J. Veh. Des.* **2005**, *38*, 290. [CrossRef]
56. Shen, X.; Feng, S.; Li, Z.; Hu, B. Analysis of Bus Passenger Comfort Perception Based on Passenger Load Factor and In-Vehicle Time. *SpringerPlus* **2016**, *5*, 62. [CrossRef]
57. Long, L.X.; Quynh, L.V.; Cuong, B.V. Study on the Influence of Bus Suspension Parameters on Ride Comfort. *Vibroeng. Procedia* **2018**, *21*, 77–82. [CrossRef]
58. Sun, R.; Wang, J.; Liu, Y. Dynamic Analysis and Seat Selection of Bus Driving Comfort under Different Road Conditions. *Appl. Sci.* **2023**, *13*, 4639. [CrossRef]
59. Le, D.; Nguyen, C.H.; Pham, T.H.N.; Nguyen, V.T.; Pham, S.M.; Le, M.T.; Nguyen, T.T. Optimizing 3D Printing Process Parameters for the Tensile Strength of Thermoplastic Polyurethane Plastic. *J. Mater. Eng. Perform.* **2023**, *32*, 10805–10816. [CrossRef]
60. Li, M.; Xu, Y.; Fang, J. Orthotropic Mechanical Properties of PLA Materials Fabricated by Fused Deposition Modeling. *Thin-Walled Struct.* **2024**, *199*, 111800. [CrossRef]
61. Sabah, F.; Wahid, A.; Kartouni, A.; Chakir, H.; ELghorba, M. Failure Analysis of Acrylonitrile Butadiene Styrene (ABS) Materials and Damage Modeling by Fracture. *Int. J. Perform. Eng.* **2019**, *15*, 2285. [CrossRef]
62. Dimic, A.; Mišković, Ž.; Jelovac, D.; Mitrović, R. Application of Rapid Prototyping in Maxillofacial Surgery. In Proceedings of the Recent Advances in Medicine and Health Sciences (RAMHS 2016), Dubai, United Arab Emirates, 21–23 January 2016.
63. Yahamed, A.; Ikonomov, P.; Fleming, P.D. Mechanical Properties of 3D Printed Polymers. *J. Print Media Technol. Res.* **2016**, *5*, 273–289. [CrossRef]
64. Sharma, G.; Kumaraswamy, A.; Patro, T.U.; Rath, S.K.; Praveen, S. Performance of Multilayer Constrained Layer Damping Structures: A Comprehensive Study Using RKU, FEM, and Experimental Approaches. *J. Vib. Eng. Technol.* **2024**, *12*, 2339–2349. [CrossRef]
65. Zhang, J.; Zhou, W.; Cao, D.; Zhang, J. A Study on the Genetic Algorithm Optimization of an Asphalt Mixture's Viscoelastic Parameters Based on a Wheel Tracking Test. *Infrastructures* **2023**, *8*, 169. [CrossRef]
66. Kumar, S.; Maheswari, S.; Singh, S.S.; Rozycki, P. Dynamic Mechanical Analysis of Epoxy Composites: Master Curve Construction and Prony Series Fitting to Investigate Filler Shape Effects on Viscoelastic Properties. *Emergent Mater.* **2025**, *8*, 5085–5097. [CrossRef]
67. Ferry, J.D. *Viscoelastic Properties of Polymers*, 3rd ed.; John Wiley & Sons: New York, NY, USA, 1980.
68. *ASTM D7028-07*; Standard Test Method for Glass Transition Temperature (DMA Tg) of Polymer Matrix Composites by Dynamic Mechanical Analysis (DMA). ASTM International: West Conshohocken, PA, USA, 2015.
69. Mandapuram, S.; Rakheja, S.; Boileau, P.-É.; Maeda, S.; Shibata, N. Apparent Mass and Seat-to-Head Transmissibility Responses of Seated Occupants under Single and Dual Axis Horizontal Vibration. *Ind. Health* **2010**, *48*, 698–714. [CrossRef]
70. Yan, L.; Gong, X. Experimental Study of Vibration Isolation Characteristics of a Geometric Anti-Spring Isolator. *Appl. Sci.* **2017**, *7*, 711. [CrossRef]
71. Hussein, M.I.; Leamy, M.J.; Ruzzene, M. Dynamics of Phononic Materials and Structures: Historical Origins, Recent Progress, and Future Outlook. *Appl. Mech. Rev.* **2014**, *66*, 040802. [CrossRef]
72. Li, Q.Q.; He, Z.C.; Li, E.; Cheng, A.G. Design and Optimization of Three-Resonator Locally Resonant Metamaterial for Impact Force Mitigation. *Smart Mater. Struct.* **2018**, *27*, 095015. [CrossRef]
73. Wang, K.; Zhou, J.; Tan, D.; Li, Z.; Lin, Q.; Xu, D. A Brief Review of Metamaterials for Opening Low-Frequency Band Gaps. *Appl. Math. Mech.-Engl. Ed.* **2022**, *43*, 1125–1144. [CrossRef]
74. Liu, Z.; Zhang, X.; Mao, Y.; Zhu, Y.Y.; Yang, Z.; Chan, C.T.; Sheng, P. Locally Resonant Sonic Materials. *Science* **2000**, *289*, 1734–1736. [CrossRef] [PubMed]
75. Zheng, X.; Lee, H.; Weisgraber, T.H.; Shusteff, M.; DeOtte, J.; Duoss, E.B.; Kuntz, J.D.; Biener, M.M.; Ge, Q.; Jackson, J.A.; et al. Ultralight, Ultrastiff Mechanical Metamaterials. *Science* **2014**, *344*, 1373–1377. [CrossRef] [PubMed]
76. Yap, X.Y.; Seetoh, I.; Goh, W.L.; Ye, P.; Zhao, Y.; Du, Z.; Lai, C.Q.; Gan, C.L. Mechanical Properties and Failure Behaviour of Architected Alumina Microlattices Fabricated by Stereolithography 3D Printing. *Int. J. Mech. Sci.* **2021**, *196*, 106285. [CrossRef]
77. Ma, T.; Li, T.; Jing, G.; Liu, H.; Bi, F. Development of a Novel Seat Suspension Based on the Cubic Stewart Parallel Mechanism and Magnetorheological Fluid Damper. *Appl. Sci.* **2022**, *12*, 11437. [CrossRef]
78. Knap, L.; Makowski, M.; Siczek, K.; Kubiak, P.; Mrowicki, A. Hydraulic Vehicle Damper Controlled by Piezoelectric Valve. *Sensors* **2023**, *23*, 7. [CrossRef]
79. Heidarian, A.; Wang, X. Review on Seat Suspension System Technology Development. *Appl. Sci.* **2019**, *9*, 2834. [CrossRef]

80. Zetarmold Moldagem Por Injeção: Como Calcular o Tempo de Ciclo 2024. Available online: https://hitopindustrial.com/pt/calcular-tempo-de-ciclo-em-moldagem-por-injecao/ (accessed on 8 January 2026).
81. Selvaraj, S.K.; Raj, A.; Rishikesh Mahadevan, R.; Chadha, U.; Paramasivam, V. A Review on Machine Learning Models in Injection Molding Machines. *Adv. Mater. Sci. Eng.* **2022**, *2022*, 1949061. [CrossRef]

Disclaimer/Publisher's Note: The statements, opinions and data contained in all publications are solely those of the individual author(s) and contributor(s) and not of MDPI and/or the editor(s). MDPI and/or the editor(s) disclaim responsibility for any injury to people or property resulting from any ideas, methods, instructions or products referred to in the content.